

1 **Solar radiation estimation in West Africa: impact of dust conditions during**
2 **2021 dry season**

3

4 Léo Clauzel¹, Sandrine Anquetin¹, Christophe Lavaysse¹, Gilles Bergametti², Christel
5 Bouet^{2,3}, Guillaume Siour⁴, Rémy Lapere¹, Béatrice Marticorena⁴, Jennie Thomas¹

6

7 ¹Université Grenoble Alpes, IRD, CNRS, Grenoble-INP, IGE, 38000 Grenoble, France

8 ²LISA, Université Paris Cité and Univ Paris Est Créteil, CNRS, F-75013 Paris, France

9 ³Institut d'Ecologie et des Sciences de l'Environnement de Paris, UMR IRD 242, Univ Paris
10 Est Créteil–Sorbonne Université–CNRS–INRAE–Université Paris Cité, F-93143 Bondy,
11 France

12 ⁴LISA, Univ Paris Est Créteil, Université Paris Cité, CNRS, LISA, F-94010, Créteil, France

13

14 *Correspondence to:* Léo Clauzel (leo.clauzel@univ-grenoble-alpes.fr), Sandrine Anquetin
15 (sandrine.anquetin@univ-grenoble-alpes.fr)

16 **Abstract**

17 The anticipated increase in solar energy production in West Africa requires high-quality solar
18 irradiance estimates, which is affected by meteorological conditions and in particular the
19 presence of desert dust aerosols. This study examines the impact of incorporating desert
20 dust into solar irradiance and surface temperature estimations. The research focuses on a
21 case study of a dust event in March 2021, which is characteristic of the dry season in West
22 Africa. Significant desert aerosol emissions at the Bodele depression are associated with a
23 Harmattan flow that transports the plume westwards. Simulations of this dust event were
24 conducted using the WRF meteorological model alone, as well as coupled with the
25 CHIMERE chemistry-transport model, using three different datasets for the dust aerosol
26 initial and boundary conditions (CAM5, GOCART, MERRA2). Results show that considering
27 desert dust reduces estimation errors in global horizontal irradiance (GHI) by about 75%.
28 The dust plume caused an average 18% reduction in surface solar irradiance during the
29 event. Additionally, the simulations indicated a positive bias in aerosol optical depth (AOD)
30 and PM10 surface concentrations. The choice of dataset for initial and boundary conditions
31 minimally influenced GHI, surface temperature, and AOD estimates, whereas PM10
32 concentrations and aerosol size distribution were significantly affected. This study
33 underscores the importance of incorporating dust aerosols into solar forecasting for better
34 accuracy.

35

36 **Short summary**

37 Solar energy production in West Africa is set to rise, needing accurate solar irradiance
38 estimates, which is affected by desert dust. This work analyses a March 2021 dust event
39 using a modelling strategy incorporating desert dust. Results show that considering desert
40 dust cut errors in solar irradiance estimates by 75% and reduces surface solar radiation by
41 18%. This highlights the importance of incorporating dust aerosols into solar forecasting for
42 better accuracy.

43

44 **1. Introduction**

45 The West African region is facing significant development challenges due to global change.
46 One of these challenges is related to access to electricity, particularly through the use of
47 renewable energy. West African countries have committed to reduce their greenhouse gas
48 emissions as part of the Paris Agreement (2015). Furthermore, assessments of solar
49 resources in West Africa demonstrate the region's substantial potential, as shown by
50 Diabaté et al. (2004), Plain et al. (2019) and Yushchenko et al. (2018). The International
51 Energy Agency (IEA) projects that the installed capacity for photovoltaic (PV) power
52 generation will increase by almost 20 times from 2020 to 2030 under its Sustainable Africa
53 Scenario (IEA, 2022). PV energy is expected to experience significant growth due to its
54 competitiveness and low-carbon nature. However, solar production is highly dependent on
55 weather conditions (Dajuma et al., 2016).

56 The growth of solar energy in West Africa calls for the development of tailored tools to
57 facilitate its integration into power grids and ensure optimal operational maintenance.
58 Accurate production forecasts are required by solar power plant operators, spanning various
59 timescales, ranging from a few hours to several days. This is essential for maximising
60 production, reducing penalties linked to predicted deliverable energy, and optimising plant
61 maintenance to minimise production losses. High-quality forecasts are also crucial for
62 electricity grid operators to maintain supply-demand equilibrium and ensure system stability.
63 Therefore, the variability of energy production significantly affects them. The key

64 meteorological variables that influence photovoltaic production are the Global Horizontal
65 Irradiance (GHI) and the air temperature. These factors, which directly impact electricity
66 production and cell efficiency, often reach high levels in this region as demonstrated by
67 Dajuma et al. (2016) and Ziane et al. (2021). Their findings indicate that solar irradiance is
68 the primary factor influencing PV production, as the generated current by the photoelectric
69 effect is proportional to the irradiance. Furthermore, they demonstrate that, at the second
70 order, the air temperature affects the efficiency of solar cells, as both parameters are
71 inversely correlated.

72
73 Clauzel et al. (2024) identified desert dust aerosol as a significant source of GHI forecast
74 errors for the only two solar power plants in the Sahel region of Sococim (Senegal) and
75 Zagtoui (Burkina Faso), particularly during the dry season. Dust aerosols are a key element
76 in the West African climate and strongly influence solar farm production through their direct
77 effect (aerosol-radiation interaction (ARI), Briant et al., 2017) and indirect effects (aerosol-
78 cloud interaction (ACI), Tuccella et al., 2019) on radiation, and also through their deposition
79 on solar panels (fouling effect, Diop et al., 2020, Aidara et al., 2023). As mentioned by Kok et
80 al. (2021), the West African desert aerosol load is the highest in the world and occurs mainly
81 during the dry season. In fact, North Africa, including the Sahara, is the world's largest
82 contributor to desert dust emissions (Prospero et al., 2002), and 60% of this dust is
83 transported to the West African region (D'Almeida, 1986; Kok et al., 2021). Most dust
84 emissions are associated with synoptic-scale atmospheric dynamics such as the Harmattan
85 flow during the dry season (Klose et al., 2010). Engelstaedter and Washington (2007)
86 pointed out the importance of small-scale wind events associated with the large-scale flow,
87 especially in the Bodele depression, which is a hotspot for dust emissions (Engelstaedter et
88 al., 2006). Analysing satellite observations, Schepanski et al. (2009) show that 65% of the
89 activation of the dust source area occurred in the early morning, demonstrating the important
90 role of the breakdown of the nocturnal low-level jet. Washington and Todd (2005) confirmed
91 the importance of the Bodele low-level jets during the dry season in initiating dust emissions
92 that can be transported to the West African coast within a few days. Dust aerosol emissions
93 are also highly linked to Mesoscale Convective Systems (MCS, Marsham et al., 2008 ;
94 Bergametti et al., 2017) and to strong near-surface winds in the intertropical discontinuity
95 zone during the rainy season (Bou Karam et al., 2009).

96
97 Some studies intend to model dust events in West Africa such as Ochiegbu (2021) who
98 implemented a back-trajectories model to understand the dust event reaching Nigeria. This
99 work revealed that most of the aerosols coming to Nigeria between 2011 and 2014 were
100 originating from the Bodele Depression. Menut (2023) focused on dust forecasting during the
101 Cloud-Atmospheric Dynamics-Dust Interactions in West Africa (CADDIWA) campaign during
102 summer 2021 (Flamant et al., 2024) using the CHIMERE regional chemistry-transport model
103 (Menut et al., 2021). The model was coupled online with the Weather Research and
104 Forecasting (WRF) meteorological model (Briant et al., 2017; Tuccella et al., 2019) to
105 perform dust aerosol concentration forecasts. The results of this work provide confidence in
106 the model coupling in the region as the dust forecast quality does not decrease with time
107 over a few days. In addition, only a limited number of studies have been conducted on the
108 prediction of GHI in the West African region. Sawadogo et al. (2024) conducted an
109 evaluation of WRF-solar GHI forecast (Jimenez et al., 2016) in Ghana for the year 2021. In
110 their work, a version of the model coupled offline with Copernicus Atmosphere Monitoring
111 Service (CAMS) Aerosol Optical Depth (AOD) forecasts was considered to integrate

112 information on aerosol load. They showed that WRF-Solar outperforms in predicting GHI
113 under clear sky conditions while its performance under high aerosol levels remains poor, that
114 was mainly attributed to uncertainties in the input AOD during data assimilation within the
115 model. Close to the region of interest, for the northern Morocco area, El Alani et al. (2020)
116 compared the performance of global models (Global Forecast System, Integrated Forecast
117 System, McClear) and demonstrated their proficiency in capturing GHI hourly temporal
118 variability.

119

120 As far as our knowledge is concerned, no studies have been conducted to assess online
121 coupled simulations between a meteorological model and an aerosol life cycle model
122 representing the emissions, the transport and the deposition in West Africa to estimate solar
123 irradiance. This is despite the significant presence of desert dust, characterised by high
124 concentrations in the region. Additionally, scarce attention has been given to the significance
125 of initial and boundary conditions for conducting the aerosol model on the performance of
126 analysis simulations, and to our knowledge, investigating these aspects would represent a
127 novel contribution to research in the West African region.

128

129 Within this general context, the objectives of this study are two folds i) to evaluate the ability
130 to reproduce a dust event using a meteorological and dust life cycle model coupling
131 configuration, and ii) to investigate whether the performance of the simulations can be
132 enhanced by modifying the aerosol initial and boundary conditions employed, and to
133 estimate the uncertainty associated with this dataset selection with regard to the errors made
134 by the model. Section 2 introduces the case study, the simulation configuration, the data and
135 models selected for this work. In Section 3, the results are presented, beginning with the
136 variables of interest for solar production (GHI and surface air temperature), followed by the
137 variables associated with the desert aerosols (AOD, concentration, size distribution,
138 emissions). Section 4 gives main conclusions and draws some perspectives for this study.

139

140 **2. Material and methods**

141

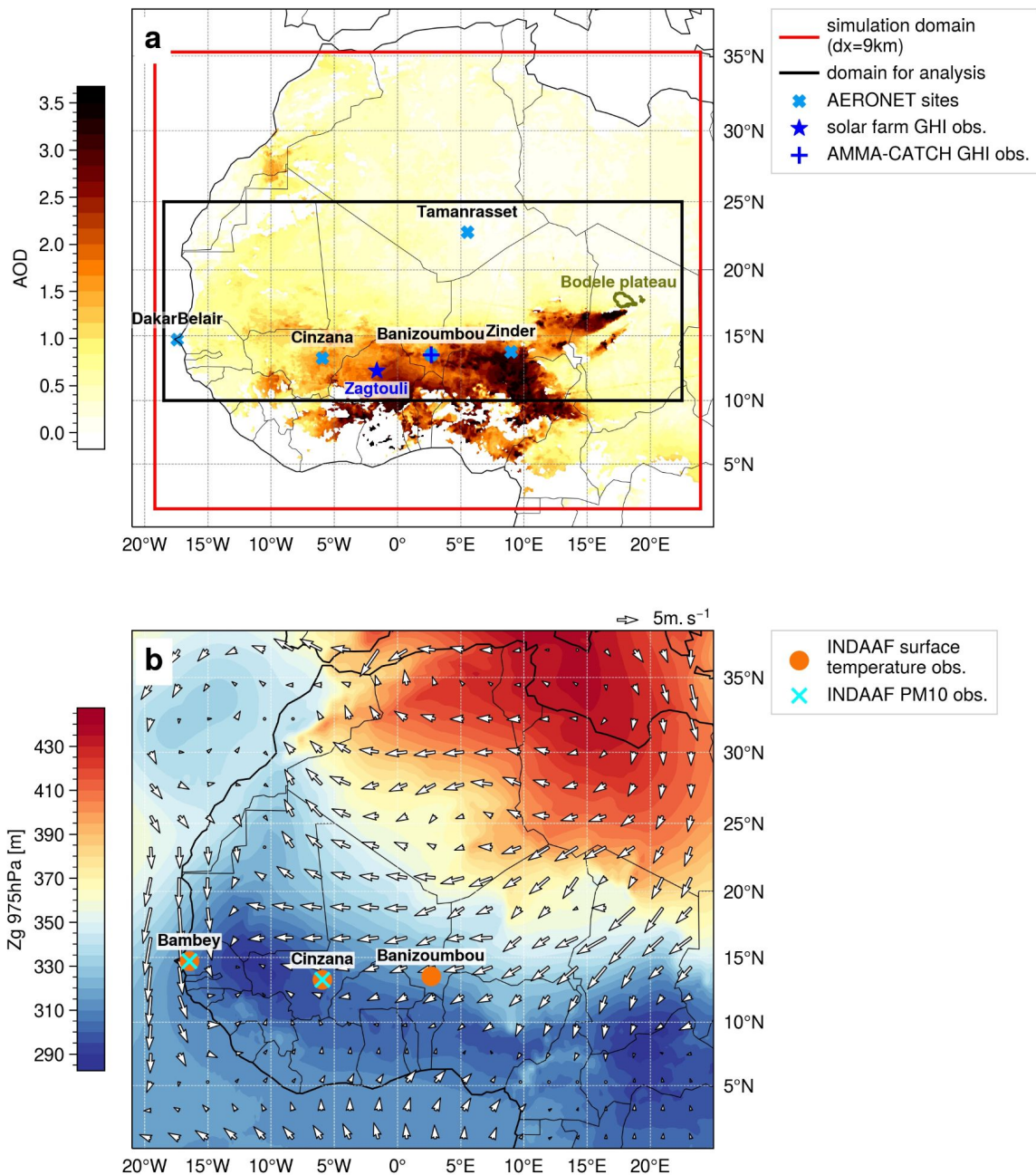
141 **2.1. Case study**

142

143 The case study is a dust event that occurs in West Africa from March 26th-00 UTC to April
144 2nd-00 UTC, 2021, i.e., during the dry season. High dust emissions occur at the Bodele
145 Depression (Chad), the plume being then transported westward. The dust plume reached its
146 maximum intensity in terms of AOD and dust concentration over West Africa, and in
147 particular over the Zagtouli solar farm (Burkina-Faso, Fig. S1), on March 30th. The event
148 was also chosen because it was not predicted in the solar forecast currently implemented for
149 the Zagtouli solar farm, leading to solar forecast errors during the passage of the dust plume
(Clauzel et al., 2024).

150

151 Figure 1 illustrates that this event is characterised by a strong Harmattan flow, with surface
152 winds from the South/South-West sweeping across the Bodele Depression (Chad), where
153 the potential for desert dust emissions is very high (Prospero et al., 2002; Washington et al.,
154 2006). Additionally, this event is characterised by a westward flow between Chad and the
155 Atlantic coast, which facilitates the transportation of the dust plume. Fig. 1a shows
156 MODerate-resolution Imaging Spectroradiometer (MODIS) satellite observations of the AOD,
157 identifying the initial dust source area on the Bodele Depression, as well as the westward
158 movement of the plume. This event is characteristic of the West African dry season
159 climatology, with a dominant Harmattan flow as described in the introduction. Figure S1
159 provides further insight into the dust plume transport during the case study.



161
 162 **Figure 1** - a) Mean aerosol Optical Depth at 550nm from MODIS satellite observations over
 163 the period 28 March-00 UTC to 02 April-00 UTC 2021. The Global Horizontal Irradiance
 164 (GHI) observations and AERONET aerosol measurement network, introduced in 2.4, are
 165 presented, as well as the boundaries of the simulated domain (red rectangle) and the area of
 166 interest for analysis (black rectangle). b) Mean synoptic conditions of the geopotential height
 167 (Zg) at 975hPa and the 10m-wind (white arrows - in m/s) over the period 28 March-00 UTC
 168 to 02 April-00 UTC 2021 from ERA5 reanalysis. The surface temperature and aerosol
 169 concentration observations from the INDAAF network, introduced in 2.4, are presented.

170

171 2.2. Modelling tools

172 In order to reproduce a dust event during the dry season in West Africa, the WRF-CHIMERE
 173 coupled model is selected as it has previously demonstrated favourable performance in

174 similar studies such as those conducted by Briant et al. (2017) and Menut (2023). The
 175 technical details of this coupled model are provided below.

176

177 **2.2.1. WRF model**

178 The meteorological Weather and Research and Forecasting model (WRF) model version
 179 3.7.1 is taken for compatibility with the CHIMERE coupling procedure. It is used in its non-
 180 hydrostatic configuration (Skamarock et al., 2008) and is forced at the boundaries of the
 181 domain every hour by the meteorological reanalysis data of ERA5 (ECMWF) provided on a
 182 regular 0.25° x 0.25° grid.

183 The model is run with a 9 km horizontal resolution, a 45s integration time step and 50
 184 vertical levels, from the surface to 50 hPa. The updated Rapid Radiative Transfer Model
 185 (RRTMG) radiation scheme (Iacono et al., 2008), which is mandatory for the aerosol optical
 186 properties feedback, is employed for both long- and short-wave radiations. Additionally, the
 187 Thompson aerosol-aware microphysics scheme (Thompson and Eidhammer, 2014) is
 188 applied. The Yonsei University planetary boundary layer's surface layer scheme (Hu et al.,
 189 2013) is also used, and the cumulus parameterisation is based on the Grell-Freitas scheme
 190 (Arakawa, 2004). The Revised MM5 surface layer scheme (Jiménez et al., 2012) is
 191 employed, while the Noah-MP Land Surface Model (Niu et al. 2011) is implemented for the
 192 land surface physics scheme.

193

194 **2.2.2. CHIMERE model**

195 The chemistry-transport model CHIMERE version v2020r3 (Menut et al., 2021) is used in
 196 conjunction with the WRF model. Both models have a 9 km horizontal grid. The CHIMERE
 197 model has 30 pressure-dependent vertical levels from the surface up to 200 hPa, with a first
 198 layer thickness of 3 hPa. The model is configured for dust-only, with no chemistry and only
 199 considering dust aerosols (details in section 2.3). The threshold friction velocities for dust
 200 emission are estimated using the Shao and Lu scheme (2000) and the 6-km spatial
 201 resolution GARLAP (Global Aeolian Roughness Lengths from ASCAT and PARASOL)
 202 dataset from Prigent et al. (2012). Mineral dust emission fluxes were calculated employing
 203 the Alfaro and Gomes (2001) scheme on 10 aerosol size bins ranging from 0.01 to 40 µm.
 204 The Fécan et al. (1999) parametrization is employed to account for the inhibitory effect of
 205 soil moisture on dust emission. Dry deposition is treated as described in Zhang et al. (2001).
 206 Wet scavenging for aerosol is computed following the Willis and Tattelman scheme (1989).
 207 The CHIMERE model includes the Fast-JX module, version 7.0b (Wild et al., 2000; Bian et
 208 al., 2002) for the calculation of radiative processes. It considers the radiative properties for
 209 each aerosol species and each aerosol size bin independently to compute the aerosol
 210 optical depths, the single scattering albedo and the aerosol asymmetry factor. More details
 211 on the dust aerosol radiative properties are given in Tables S1 and S2. Finally, we test three
 212 different initial and boundary condition datasets for mineral dust load (see 2.2.3).

213

214 **Table 1 - Parameterizations used in WRF and CHIMERE**

WRF	
microphysics	Thompson aerosol-aware (Thompson and Eidhammer, 2014)
radiation	RRTMG scheme for LW and SW (Iacono et al., 2008)

land surface	Noah-MP land surface scheme (Niu et al., 2011)
planetary boundary layer	Yonsei University scheme (Hu et al., 2013)
surface layer	Revised MM5 surface layer scheme (Jimenez et al., 2012)
cumulus	Grell-Freitas scheme (Arakawa, 2004)
CHIMERE	
threshold friction velocities	Shao and Lu (2000) scheme
soil moisture	Fécan et al. (1999) scheme
dust emission fluxes	Alfaro and Gomes (2001) scheme
radiative processes	Fast-JX model, version 7.0b (Wild et al., 2000; Bian et al., 2002)
aerosol size distribution bins (diameters in μm)	0.010 - 0.022
	0.022 - 0.048
	0.048 - 0.107
	0.107 - 0.235
	0.235 - 0.516
	0.516 - 1.136
	1.136 - 2.500
	2.500 - 5.000
5.000 - 10.00	
10.00 - 40.00	

215

216

2.2.3. Dust aerosol initial and boundary condition datasets

217 In this study, the uncertainty in the solar estimate associated with the initial and boundary
 218 conditions of the dust aerosol load is evaluated. Three datasets were used: a climatology
 219 derived from the Global Ozone Chemistry Aerosol Radiation and Transport (GOCART,
 220 Ginoux et al., 2001), the Modern-Era Retrospective analysis for Research and Applications
 221 Version 2 (MERRA2) reanalysis (Gelaro et al., 2017) and the CAMS reanalysis (Inness et
 222 al., 2019).

223 The GOCART climatology is provided with the distribution of the CHIMERE model. It is a
 224 monthly climatology on a coarse horizontal grid ($2^\circ \times 2.5^\circ$), which is corrected by applying a
 225 factor of 0.3 as in Vautard et al. (2005).

226 The MERRA2 reanalysis combines the Goddard Earth Observing System (GEOS) and
 227 GOCART models, which are online coupled and implemented with a data assimilation
 228 system. It has a 3-hour temporal resolution and is presented on a $0.5^\circ \times 0.635^\circ$ horizontal
 229 grid. The observational data considered in the data assimilation process are AOD satellite
 230 observations from MODIS, Advanced Very High Resolution Spectroradiometer (AVHRR),
 231 Multi-angle Imaging SpectroRadiometer (MISR) and ground observations from the AEROSOL
 232 RObotic NETwork (AERONET).

233 The CAMS reanalysis was constructed using 4DVar data assimilation in ECMWF's
 234 Integrated Forecast System (IFS). It has a temporal resolution of 3 hours and is computed
 235 on a regular 0.75° horizontal grid. The AOD data from the Visible Infrared Imaging
 236 Radiometer Suite (VIIRS), the MODIS and the Infrared Atmospheric Sounding Interferometer
 237 (IASI) satellite observations are used as observational information in the data assimilation
 238 process. The version 48R1 of CAMS is used in this study.

239 These three dust aerosol initial and boundary datasets differ in type (climatological or
 240 reanalysis), in horizontal, vertical and temporal resolution, and in the resolution and range of
 241 their aerosol size distribution. While GOCART has the highest number of aerosol classes
 242 with 7 bins, CAMS covers a wider size spectrum despite a lower size resolution with only 3
 243 classes. MERRA2 has an intermediate resolution with 5 classes, but covers a smaller
 244 particle size spectrum than CAMS. The CHIMERE model pre-processes these dust aerosol
 245 size distributions by applying a transfer coefficient δ to compute the dust aerosol
 246 concentration on the 10 aerosol size bin defined for the simulations :

$$c_j = \sum_i \delta_{i,j} \times c_i \quad (1)$$

247 where c_i is the dust aerosol concentration of the i^{th} size bin from the initial and boundary
 248 condition dataset considered, c_j is the dust aerosol concentration of the j^{th} size bin in the
 249 CHIMERE simulation, and $\delta_{i,j}$ is the transfer coefficient. This transfer coefficient is derived
 250 as :

- 251 - $\delta_{i,j}=0$ if the i^{th} size bin from the initial and boundary condition dataset is found to be
 252 wholly outside the j^{th} size bin in the CHIMERE simulation;
- 253 - $\delta_{i,j}=1$ if the i^{th} size bin from the initial and boundary condition dataset is wholly
 254 encompassed by the j^{th} size bin in the CHIMERE simulation;
- 255 - $\delta_{i,j} = \frac{\log(r_{j,max}) - \log(r_{j,min})}{\log(R_{i,max}) - \log(R_{i,min})}$ if the i^{th} size bin from the initial and boundary condition
 256 dataset wholly encompasses the j^{th} size bin in the CHIMERE simulation;
- 257 - $\delta_{i,j} = \frac{\log(R_{i,max}) - \log(r_{j,min})}{\log(R_{i,max}) - \log(R_{i,min})}$ if the i^{th} size bin from the initial and boundary condition
 258 dataset partially overlaps the j^{th} size bin in the CHIMERE simulation, but extends
 259 below the start of this size bin;
- 260 - $\delta_{i,j} = \frac{\log(r_{j,max}) - \log(R_{i,min})}{\log(R_{i,max}) - \log(R_{i,min})}$ if the i^{th} size bin from the initial and boundary condition
 261 dataset partially overlaps the j^{th} size bin in the CHIMERE simulation, but extends
 262 beyond the end of this size bin;

263 where $R_{i,min}$ and $R_{i,max}$ are respectively the radius of the lower and upper limit of the i^{th} size
 264 bin from the initial and boundary condition dataset, and $r_{j,min}$ and $r_{j,max}$ are respectively the
 265 radius of the lower and upper limit of the j^{th} size bin in the CHIMERE simulation.

266
 267 For the sake of simplicity, throughout this article, we will refer to the WRF-CHIMERE
 268 simulations runned with the GOCART, the MERRA2, and the CAMS dust aerosol initial and
 269 boundary conditions as *wrf_chimere-G*, *wrf_chimere-M*, and *wrf_chimere-C* simulations
 270 respectively.

271 Table 2 summarises the characteristics of the three dust aerosol datasets and their
 272 associated size distributions.

273

274 **Table 2.** Summary of the characteristics of the dust initial and boundary condition products.

	GOCART	MERRA2	CAMS
type	climatology	reanalysis	reanalysis
temporal resolution	monthly	3h	3h
vertical levels	20	72	60
horizontal resolution (lat x lon)	2°x2.5°	0.5°x0.635°	0.75°x0.75°
dust aerosol size distribution (radius in µm)	0.20 - 0.36 µm	0.1 - 1.0 µm	0.03 - 0.55 µm
	0.36 - 0.60 µm	1.0 - 1.8 µm	0.55 - 0.90 µm
	0.60 - 1.20 µm	1.8 - 3.0 µm	0.90 - 20.00 µm
	1.20 - 2.00 µm	3.0 - 6.0 µm	
	2.00 - 3.60 µm	6.0 - 10.0 µm	
	3.60 - 6.00 µm		
	6.00 - 12.00 µm		

275

276

2.3. Modelling strategy

277 The domain of simulation extends from 2° to 35°N and from 19°W to 24°E, as illustrated by
 278 the red box in Figure 1b. The domain is large enough to represent the primary atmospheric
 279 flows, including the Harmattan North/North-West flow and the monsoon South flow, as well
 280 as the transport of the emitted aerosol plumes. A horizontal resolution of 9 km has been
 281 selected in order to ensure that the grid ratio is approximately 3 with the ERA5
 282 meteorological forcing. This choice is also motivated by the a priori intention to achieve a
 283 resolution higher than that of previous CHIMERE simulations performed in this region and
 284 compared to the operational solar forecast model used for the Zagtoui solar farm, which are
 285 based on global forecast models (see 2.4.1). The CHIMERE model is configured in a “dust
 286 only” model, which models only the mineral dust type. This hypothesis is supported for this
 287 dust case study by Fig. S2, as desert dust is the dominant aerosol during the event,
 288 particularly above 10°N. This hypothesis is also reinforced by the dust optical depth (DOD)
 289 to AOD ratio derived from the CAMS reanalysis, which exceeds 80% during this case study
 290 and for the domain of interest (not shown). It is notable that biomass burning, which
 291 represents the other principal aerosol source in this region, is no longer a significant
 292 contributor to aerosol levels at that time of the year (Evans et al., 2018).

293 The WRF and CHIMERE models are coupled online through the OASIS3 MCT coupler. A
 294 two-way coupling strategy is selected, in which WRF sends meteorological variables to
 295 CHIMERE which in turn exchanges aerosol information such as AOD, Single Scattering
 296 Albedo (SSA) and Asymmetry Factor. This coupling strategy imposes most of the WRF
 297 parameterisations. The exchange frequency is set to 15 minutes. The WRF model computes

298 fields on 50 levels, which are linearly interpolated over the 30 CHIMERE vertical levels via
299 the OASIS coupler. The coupling includes the feedbacks of aerosol-radiation interactions
300 (ARI, direct aerosol effect) and aerosol-cloud interactions (ACI, indirect aerosol effects)
301 simultaneously.

302 The simulation starts on March 14th-00 UTC and ends on April 2nd-00 UTC, 2021. The first
303 two weeks served as the spin-up period. The simulation outputs are analysed for the period
304 of March 28th-00 UTC to April 2nd-00 UTC, which corresponds to the passage of the
305 dust plume in the Sahel region, in particular around the Zagtouli solar farm in Burkina Faso.
306 Four simulations were conducted: a meteorological simulation using WRF model alone, and
307 dust simulations with the coupled WRF-CHIMERE models using as initial and boundary
308 conditions the GOCART climatology, the MERRA2 reanalysis and the CAMS reanalysis. The
309 simulation using only WRF allows for the evaluation of the impact of taking into account dust
310 aerosols in estimating solar irradiance. This is compared to the other three simulations,
311 which are also used to evaluate the uncertainties associated with the choice of the aerosol
312 initial and boundary condition dataset. A domain of interest, spanning 10°N to 25°N (Fig. 1a),
313 was selected for analysis and comparisons. This choice was guided by the dust plume
314 trajectory (Fig. S1) and the “dust only” hypothesis (Fig. S2).

315

316 **2.4. Evaluation datasets**

317 This section presents the local and regional data that are employed in the evaluation of the
318 simulations.

319

319 **2.4.1. GHI**

320 The Global Horizontal Irradiance (GHI) is the total shortwave irradiance from the Sun on a
321 horizontal surface on Earth. It is the sum of direct irradiance, which takes into account the
322 solar zenith angle, and diffuse horizontal irradiance. It is measured in $W.m^{-2}$ for the
323 wavelength range 0.3 - 3.0 μm .

324

325 The national electricity company of Burkina-Faso, Sonabel, operates a solar farm in Zagtouli
326 (12.31°N;1.64°W; Fig. 1a), approximately 15 km west of the capital, Ouagadougou. It has an
327 installed capacity of 34 MWp and contributes up to 4% of Burkina Faso's annual electricity
328 production. Ground GHI measurements from pyranometers are available at a temporal
329 resolution of 15 minutes for the Zagtouli solar plant and undergo pre-processing to ensure
330 quality control. This involves removing outliers and days with missing data, visually checking
331 the consistency of the measured values and selecting data corresponding to production
332 hours (positive values for solar irradiance at the top of the atmosphere). Operational GHI
333 forecasts for this solar farm are computed by the French company Steadysun. These
334 forecasts are based on a multi-model, multi-member and multi-mesh grid aggregation, which
335 is derived from the NCEP Global Ensemble Forecast System and the ECMWF Integrated
336 Forecast System (Clauzel et al., 2024).

337 In-situ measurements of GHI from pyranometers (Fig. 1a) are also available at a 15-minutes
338 temporal resolution for the Banizoumbou (Niger) surface station, installed as part of the
339 AMMA-CATCH observatory (Analyse Multidisciplinaire de la Mousson Africaine - Couplage
340 de l'Atmosphère Tropicale et du Cycle Hydrologique, AMMA-CATCH (2005)).

341 The two measurement sites were selected because they are the only locations where GHI
342 observations have been made available along the dust plume transport for the case study,
343 with the Zagtouli power station being one of the first large solar farms in West Africa and the
344 AMMA-CATCH observatory being the only one to offer continuous GHI measurements for
345 the region and period of interest.

346

347 The CAMS gridded solar radiation dataset (CAMS solar radiation services v4.6, Schroedter-
348 Homscheidt et al., 2022), based on the Heliosat-4 method (Qu et al., 2017), provides several
349 variables related to solar irradiance, such as clear-sky and all-sky GHI. It has a horizontal
350 resolution of $0.1^\circ \times 0.1^\circ$ and provides data every 15 minutes. The clear sky model includes
351 aerosols through the CAMS chemical transport model (Inness et al., 2019), which integrates
352 data assimilation of AOD and is coupled online to a numerical weather prediction model.
353 Cloud information for the all-sky model is derived from MeteoSat Second Generation (MSG)
354 satellite observations using the AVHRR Processing scheme Over cLOUDs, Land and Ocean
355 (APOLLO) Next Generation cloud processing scheme (Kl user et al., 2015). The dataset was
356 selected for comparison with the simulations as it integrates a description of aerosol
357 processes. While Yang and Bright (2020) and Sawadogo et al. (2023) show that it is the best
358 performing product for estimating surface solar irradiance in the West African region among
359 several satellite-based gridded irradiance products, this dataset still has a negative bias of
360 about 10% for all-sky solar irradiance estimates at desert stations in North Africa (CAMS
361 solar radiation regular validation report, Lef vre, 2022).

362

363

2.4.2. Surface temperature

364 In-situ surface temperature measurements are available for three stations of the
365 International Network to study Deposition and Atmospheric composition in Africa (INDAAF) :
366 Banizoumbou (Niger, 13.54° N, 2.66° E, 6.2m above surface; Rajot et al, 2010a; Marticorena
367 et al, 2010; Kaly et al., 2015), Cinzana (Mali, 13.28° N, 5.93° W, 2m above surface; Rajot et
368 al, 2010b; Marticorena et al, 2010; Kaly et al., 2015) and Bambey (Senegal, 14.70° N,
369 16.47° W, 5.2m above surface; Marticorena et al, 2021a) (Fig. 1b). The measurement sites
370 were selected since they are almost aligned around $13\text{-}15^\circ$ North, which represents the main
371 pathway of Saharan and Sahelian dust towards the Atlantic Ocean during the case study.
372 The ERA5 atmospheric reanalysis (Hersbach et al., 2020) provides spatially continuous
373 hourly values of surface temperature at 2 metres and has a horizontal resolution of $0.25^\circ \times$
374 0.25° .

375

376

2.4.3. Aerosol

377 The INDAAF network also provides data on aerosol concentration through ground
378 measurements of PM_{10} , i.e. the concentration of atmospheric particles having an
379 aerodynamic diameter less than $10 \mu\text{m}$. For this case study, hourly PM_{10} measurements are
380 available for two stations (Fig. 1b): Cinzana (Rajot et al, 2010c; Marticorena et al, 2021; Kaly
381 et al, 2015) and Bambey (Marticorena et al, 2021b).

382 The CAMS atmospheric reanalysis (Inness et al., 2019) is also used to evaluate regional
383 surface PM_{10} concentration and AOD. It provides 3-hourly data with a horizontal resolution of
384 $0.75^\circ \times 0.75^\circ$, with a surface layer thickness of 2.4 hPa.

385

386 Local ground measurements of AOD are retrieved from the AErosol RObotic NETwork level
387 1.5 dataset (AERONET, Holben et al., 1998; Giles et al., 2019). AOD is calculated from sun
388 photometer recordings, along with Ångstr m Exponent, and is only available during clear sky
389 conditions in daylight hours, with a resolution of 1 minute. The AOD at 400 nm simulated
390 with the WRF-CHIMERE model is converted to 440 nm for comparison with AERONET,
391 using the Ångstr m formula :

$$\frac{AOD_{\lambda}}{AOD_{\lambda_0}} = \left(\frac{\lambda}{\lambda_0} \right)^{-\alpha} \quad (2)$$

392 where AOD_{λ} is the AOD at the desired wavelength, $\lambda=440\text{ nm}$ here ; AOD_{λ_0} is the AOD at
 393 the wavelength simulated in the model, $\lambda_0=400\text{ nm}$ here ; α is the Ångström exponent,
 394 derived from the simulated AOD at different wavelengths and here given for the range from
 395 400 nm to 600 nm.

396

397 AERONET also provides an aerosol size distribution dataset estimated through inversion of
 398 the photometers data, as described in Dubovik and King (2000). The algorithm for inversion
 399 provides a volume particle size distribution for 22 bins, which are logarithmically distributed
 400 for radii between 0.05 μm and 15 μm . For comparison with the modelled aerosol size
 401 distribution, this distribution is interpolated on the CHIMERE simulated aerosol size
 402 distribution which is composed of 10 bins ranging from 0.01 μm to 40.00 μm in diameter (see
 403 Table 1). Given that the coarsest bin (10.00-40.00 μm) is at the limit of the capabilities of the
 404 inversion method, and the two thinnest bins (0.010-0.022 μm and 0.022-0.048 μm) are out of
 405 the range of the inversion product, the AERONET dataset size sections are interpolated on
 406 the CHIMERE size sections ranging from 0.048 to 10.0 μm . Consequently, only comparisons
 407 between the three simulations can be made for the three size sections which are out of the
 408 range of AERONET product. The column aerosol volume size distribution simulated by the
 409 model is calculated for each bin “ i ” as in Menut et al. (2016) :

$$\frac{dV(r_i)}{d \ln(r_i)} = \sum_{k=1}^{nlevels} \frac{m_{k,r_i} \times \Delta z_k}{\rho_{dust} \times \ln(r_{i,max}/r_{i,min})} \quad (3)$$

410 where r_i is the mean mass median radius (in μm) and $r_{i,min}$ and $r_{i,max}$ the boundaries of the
 411 i^{th} bin. m_{k,r_i} is the dust aerosol mass concentration (the mass of aerosol in one cubic metre
 412 of air, in $\mu\text{g} \cdot \text{m}^{-3}$). ρ_{dust} is the dust aerosol density (the mass of the particle in its own volume,
 413 $\rho_{dust}=2300\text{ kg} \cdot \text{m}^{-3}$). Δz_k is the model layer thickness (in metres), for a total of n levels (here
 414 30 vertical levels).

415

416 The locations of the five AERONET sites used for comparison in this study are illustrated in
 417 Figure 1a.

418

419 The spatially continuous AOD is also derived from level 2 aerosol products of MODIS Terra
 420 and Aqua satellites (combined Dark Target, Deep Blue AOD at 0.55 micron, Collection 6.1,
 421 Platnick et al., 2015). It provides a measure of the AOD at 550 nm during daytime for clear
 422 sky conditions, with a spatial resolution of 10 km. To compare simulated AOD from WRF-
 423 CHIMERE models with AOD from MODIS, the former is converted from 600 nm to 550 nm.
 424 The conversion is performed using the Ångström formula (eq. 2).

425

426 Table 3 provides a general overview of the data used to evaluate the simulations in this
 427 study.

428

429 **Table 3** - Summary of data used to evaluate the simulations.

product	type	resolution
---------	------	------------

	Zagtouli solar farm monitoring system	pyranometer GHI measurement	local
GHI	AMMA-CATCH observational network	pyranometer GHI measurement	local
	CAMS gridded solar radiation	atmospheric reanalysis	0.01°x0.01°
	INDAAF network	ground measurements	local
temperature	ERA5	atmospheric reanalysis	0.25°x0.25°
	INDAAF network	ground measurements	local
PM₁₀	CAMS (v48R1, EAC4)	atmospheric reanalysis	0.75°x0.75°
Aerosol Size Distribution	AERONET network	inversion product	local
	AERONET network	sunphotometer ground measurements	local
Aerosol Optical Depth	MODIS	satellite observations	10km

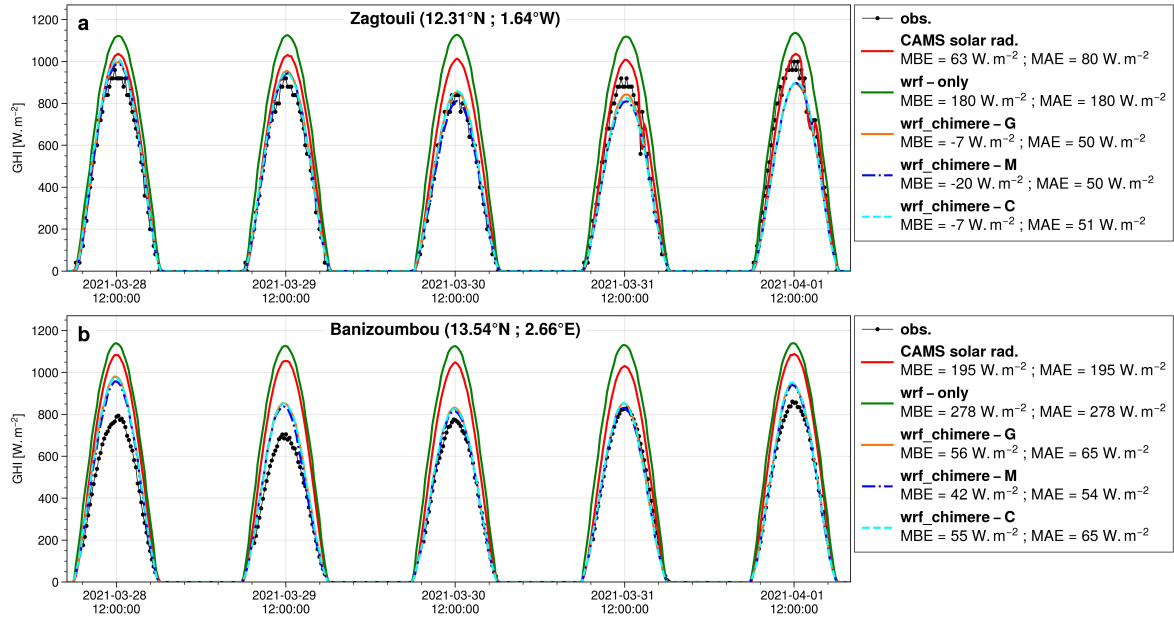
430

431 **3. Results**

432 The analysis starts by assessing the errors and uncertainties associated with the dust
 433 aerosol initial and boundary condition dataset employed to estimate the variables of interest
 434 for solar production, i.e. GHI and surface temperature. Subsequently, we investigate the
 435 potential causes of these uncertainties by evaluating the AOD, aerosol size distribution, and
 436 surface aerosol concentration (PM₁₀), as well as by examining mineral dust emissions and
 437 the flux of these aerosols at the boundaries of the domain. The metrics used to assess the
 438 quality of the simulations are described in Supplementary Materials.

439

440 **3.1. GHI**



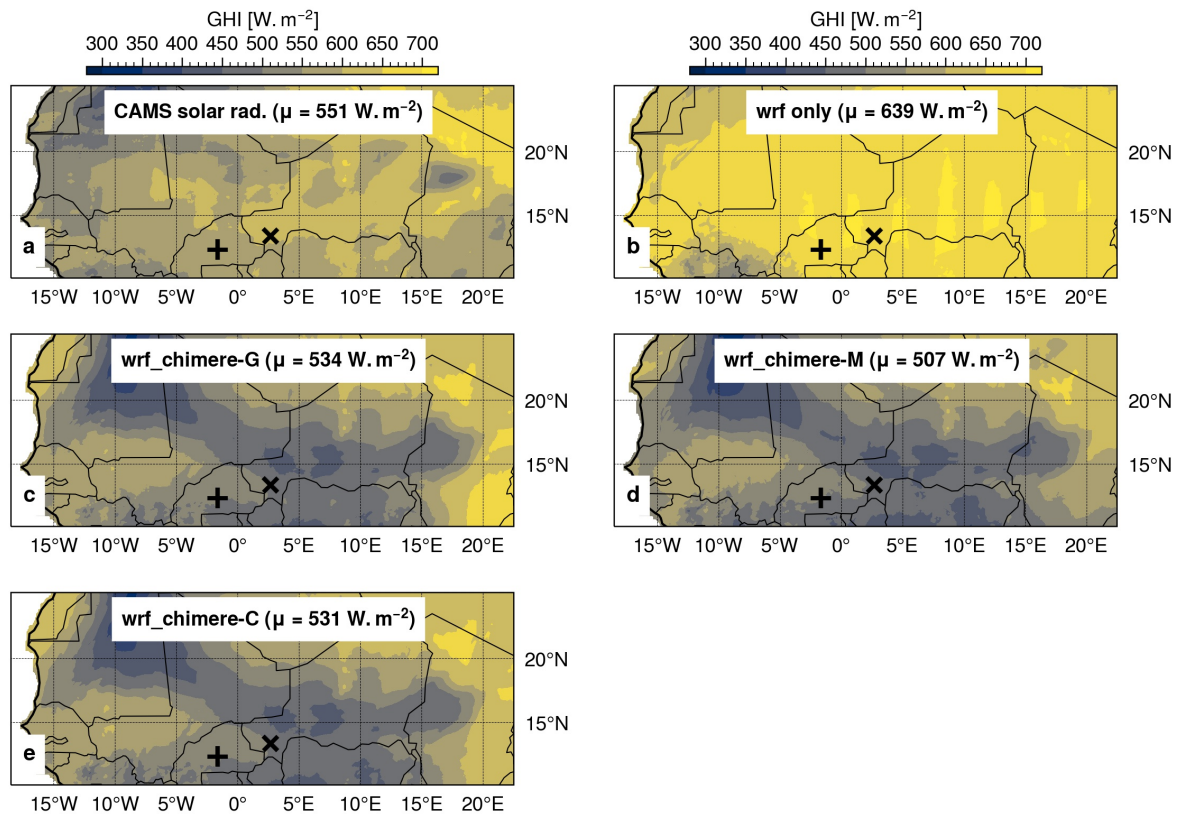
441
 442 **Figure 2** - Local comparison of CAMS gridded solar radiation product and simulated GHI
 443 against a) the Zagtouli solar farm observations and b) the Banizoumbou AMMA-CATCH
 444 observations. *wrf_chimere-G*, *wrf_chimere-M* and *wrf_chimere-C* refer to the WRF-
 445 CHIMERE simulations using GOCART, MERRA2 and CAMS as dust aerosol initial and
 446 boundary condition dataset respectively.

447
 448 In Fig. 2, the local evaluation demonstrates the effect of taking into account dust aerosol for
 449 GHI estimation with the WRF-CHIMERE coupling over the WRF meteorological model
 450 alone. The coupling reduces the MAE by a factor of 3.6 at Zagtouli and by a factor of 4.6 at
 451 Banizoumbou on average. The simulations accurately represent the reduction in GHI
 452 intensity caused by the dust plume at both stations. However, the reduction persists
 453 compared to the observations at Zagtouli. At Banizoumbou, the simulations overestimate
 454 GHI at the beginning and end of the case study.

455 Figure 2 also indicates that the CAMS gridded solar radiation product fails to fully reproduce
 456 the dust event, with only a small reduction in GHI during the passage of the dust plume and
 457 an intermediate MAE between the WRF only and the WRF-CHIMERE simulations. This point
 458 serves to highlight the advantages of using a regional model in comparison to a global
 459 product for the simulation of dust conditions and the estimation of solar irradiance.

460 Furthermore, the uncertainty in GHI estimation related to the choice of the dust aerosol initial
 461 and boundary condition dataset is limited, particularly when compared to the errors. This is
 462 evidenced by the fact that the mean standard deviation between the three WRF simulations
 463 is only 7% of the average MAE of these simulations at Zagtouli, and only 5% at
 464 Banizoumbou.

465



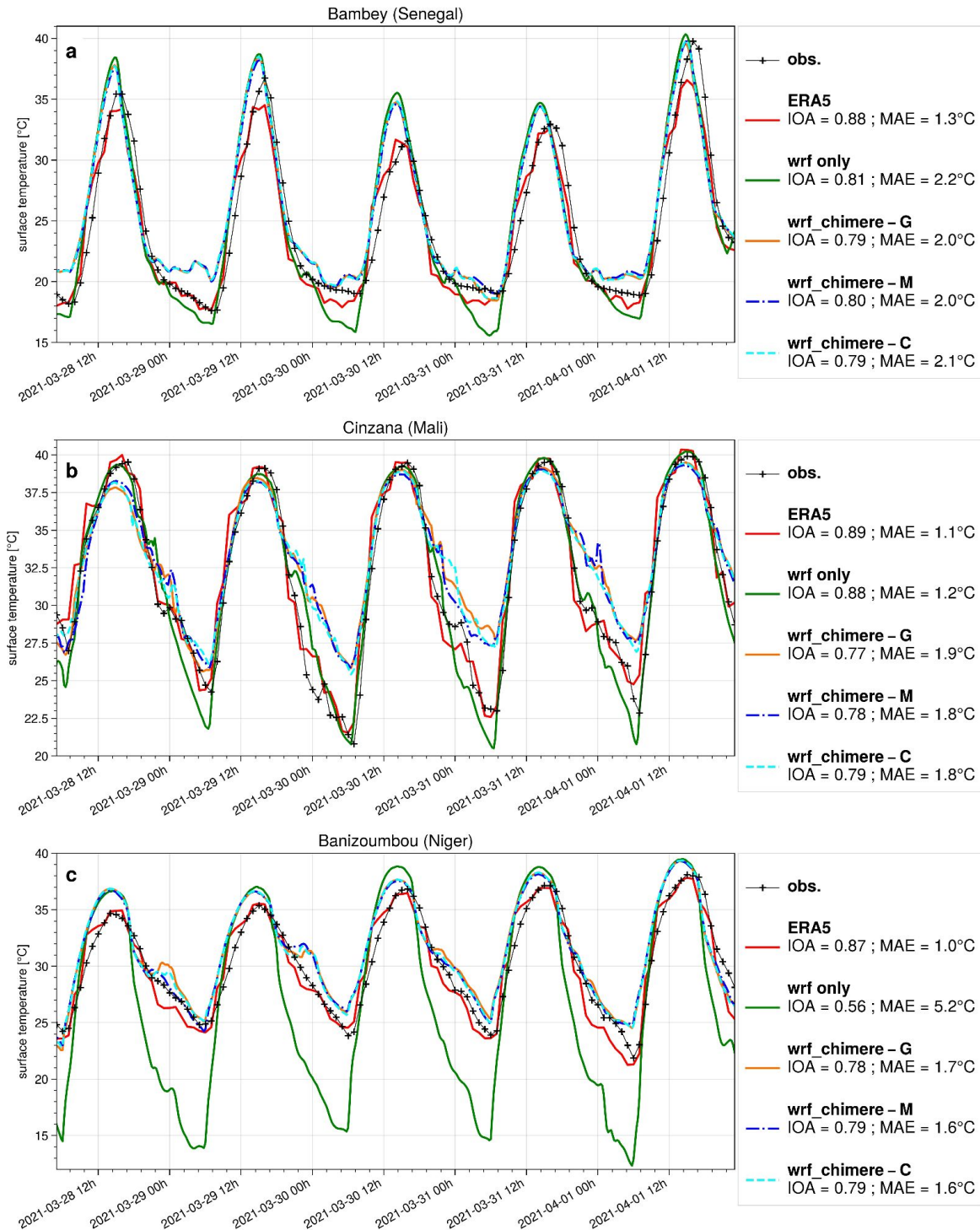
466
 467 **Figure 3** - Mean day-time GHI during the period of 28 March-00 UTC to 02 April-00 UTC
 468 2021 as estimated by a) the CAMS gridded solar radiation dataset, b) the WRF only
 469 simulation, and the WRF-CHIMERE simulations with c) GOCART, d) MERRA2 and e)
 470 CAMS as dust aerosol initial and boundary condition dataset; + is the Zagtoui solar farm
 471 and x is the Banizoumbou site. μ is the mean GHI estimates over the domain.

472
 473 The regional comparison presented in Fig. 3 provides more insight into the impact of
 474 incorporating dust on GHI estimation with the WRF-CHIMERE coupling, when compared to
 475 the WRF meteorological model alone. As anticipated the WRF-only simulation has the
 476 highest GHI estimates. The WRF-CHIMERE simulations indicate that dust aerosols reduce
 477 the mean GHI estimation by approximately $115 W \cdot m^{-2}$ (-18%) as compared to the WRF-only
 478 simulation, while the CAMS gridded solar radiation global product shows a reduction of
 479 $88 W \cdot m^{-2}$ (-14%). The three WRF-CHIMERE simulations exhibit identical regional patterns,
 480 with lower mean GHI values observed on the dust plume trajectory from the Bodele
 481 Depression to the West, and also in the South Atlas region. In contrast, the CAMS gridded
 482 solar radiation dataset does not show this regional pattern, which may indicate that this
 483 global product does not fully capture the dust event.

484 Furthermore, the uncertainty in GHI estimation associated with the choice of the dust aerosol
 485 initial and boundary conditions dataset is limited, particularly when compared to the changes
 486 brought by the taking of dust aerosol into account. Indeed, the standard deviation between
 487 the three WRF-CHIMERE simulations represents only 5% of the mean difference between
 488 these three simulations and the WRF-only simulation without dust.

489
 490

3.2. Temperature



491

492 **Figure 4** - Local comparison of ERA5 and simulated surface temperature with the INDAAF
 493 observations for a) Bambey (Senegal), b) Cinzana (Mali) and c) Banizoumbou (Niger)
 494 measurement sites. *wrf_chimere-G*, *wrf_chimere-M* and *wrf_chimere-C* refer to the WRF-
 495 CHIMERE simulations using GOCART, MERRA2 and CAMS as dust aerosol initial and
 496 boundary condition dataset respectively. *IOA* is the Indicator of Agreement and *MAE* is the
 497 Mean Absolute Error.

498

499 Figure 4 illustrates the contrasting outcomes of taking into account dust aerosols into the
 500 WRF-CHIMERE coupling in comparison to the WRF meteorological model alone for the

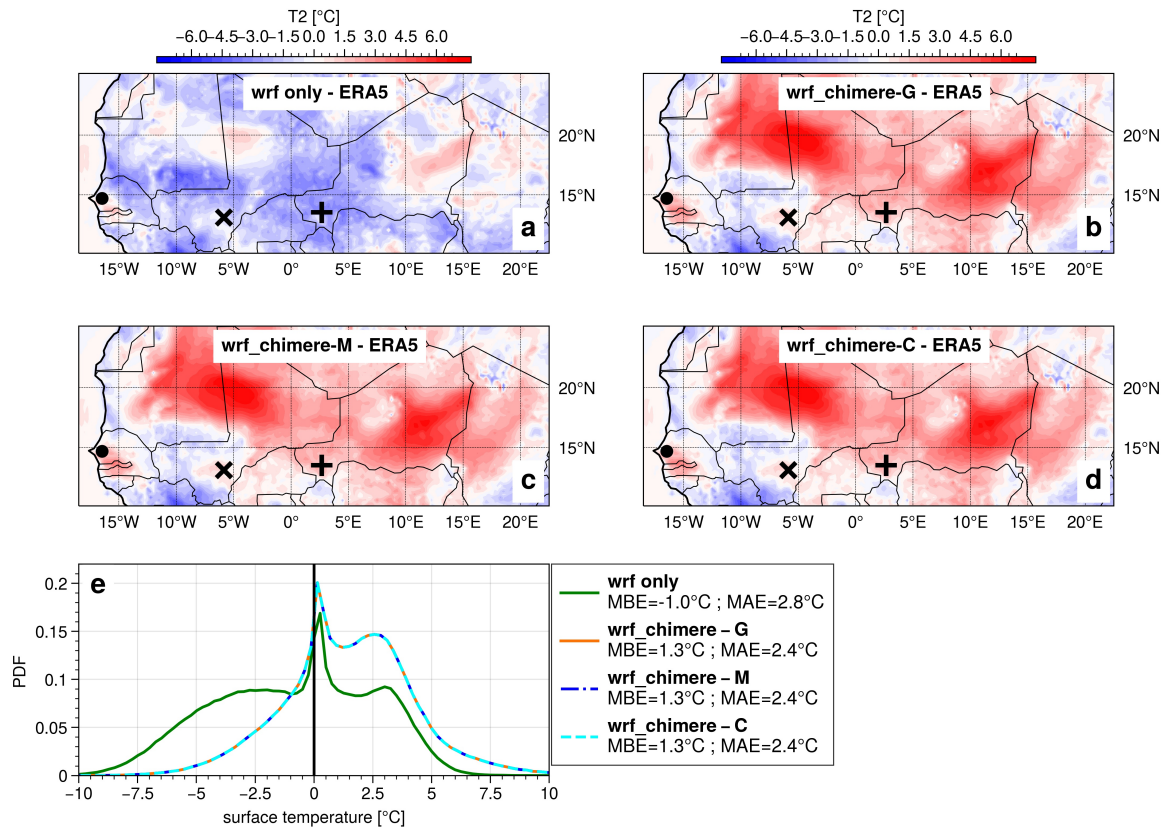
501 estimation of surface temperature. At Bambey (Fig. 4a), which is far from the dust source
502 areas, the coupling has no effect on daytime temperatures but does affect night-time
503 temperatures. The WRF-CHIMERE and WRF-only simulations have IOA and MAE of the
504 same order of magnitude. At Cinzana (Fig. 4b), the WRF-only simulation performed better,
505 with a MAE 0.6°C lower than the coupled simulations, especially for night-time temperatures
506 but also for estimating the daily temperature peak. Finally, at Banizoumbou (Fig. 4c), which
507 is near the dust source areas, the coupling leads to a significant improvement in surface
508 temperature estimation, with an IOA of approximately 0.79 compared to 0.56 for the WRF-
509 only simulation and a MAE reduced by around 3.6°C. The impact of dust aerosols on
510 temperature is particularly pronounced at night-time. However, dust also affects the daily
511 temperature peak, with a reduction of 1.1°C of the daily maximum temperature observed on
512 the 30th of March.

513 Depending on the position of the measurement station, the results show a contrast, with a
514 significant improvement with the model coupling close to the source zones at Banizoumbou.
515 However, this improvement is reversed with increasing distance at Cinzana. This suggests
516 errors in the simulation of the transport of the dust plume from the source zones (Bodele
517 Depression) towards the West. Overall, the main differences between WRF only and WRF-
518 CHIMERE coupled simulations occur at night time when there is no solar production. These
519 differences highlight the warming effect due to the dust aerosol interaction with the longwave
520 earth radiation.

521 In general, the uncertainty associated with the choice of the dust aerosol initial and boundary
522 condition dataset for the WRF-CHIMERE simulations is negligible compared to the errors in
523 temperature estimation or the difference with the WRF-only simulation.

524 The value of the ERA5 reanalysis for surface temperature evaluation is also reinforced in
525 Fig. 4, since it shows the lowest MAE and highest IOA. This dataset can therefore be
526 considered reliable for a regional evaluation of surface temperature.

527



528
 529 **Figure 5** - Mean difference in surface temperature as compared to the ERA5 reanalysis for
 530 a) the WRF only simulation, the WRF-CHIMERE simulations with b) GOCART, c) MERRA2
 531 and d) CAMS as dust aerosol initial and boundary condition dataset, during the period of 28
 532 March-00 UTC to 02 April-00 UTC 2021; the black point is the Bambey, x is the Cinzana and
 533 + is the Banizoumbou INDAAF sites. e) Probability Density Function for the differences in
 534 surface temperature between simulations and the ERA5 reanalysis.

535
 536 The regional surface temperature evaluation in Fig. 5 also reveals a contrast benefit of the
 537 coupling approach for the surface temperature estimation. While the WRF alone simulation
 538 (Fig. 5a) underestimates the surface temperature all over the domain, WRF-CHIMERE
 539 simulations are overestimating surface temperature in the dusty areas (Saharan region, Fig.
 540 5bcd). Overall, taking into account dust aerosol in the estimation of surface temperature
 541 reduces the MAE by 14% (Fig. 5e) when comparing the surface temperature estimates from
 542 simulations with the ERA5 reanalysis.

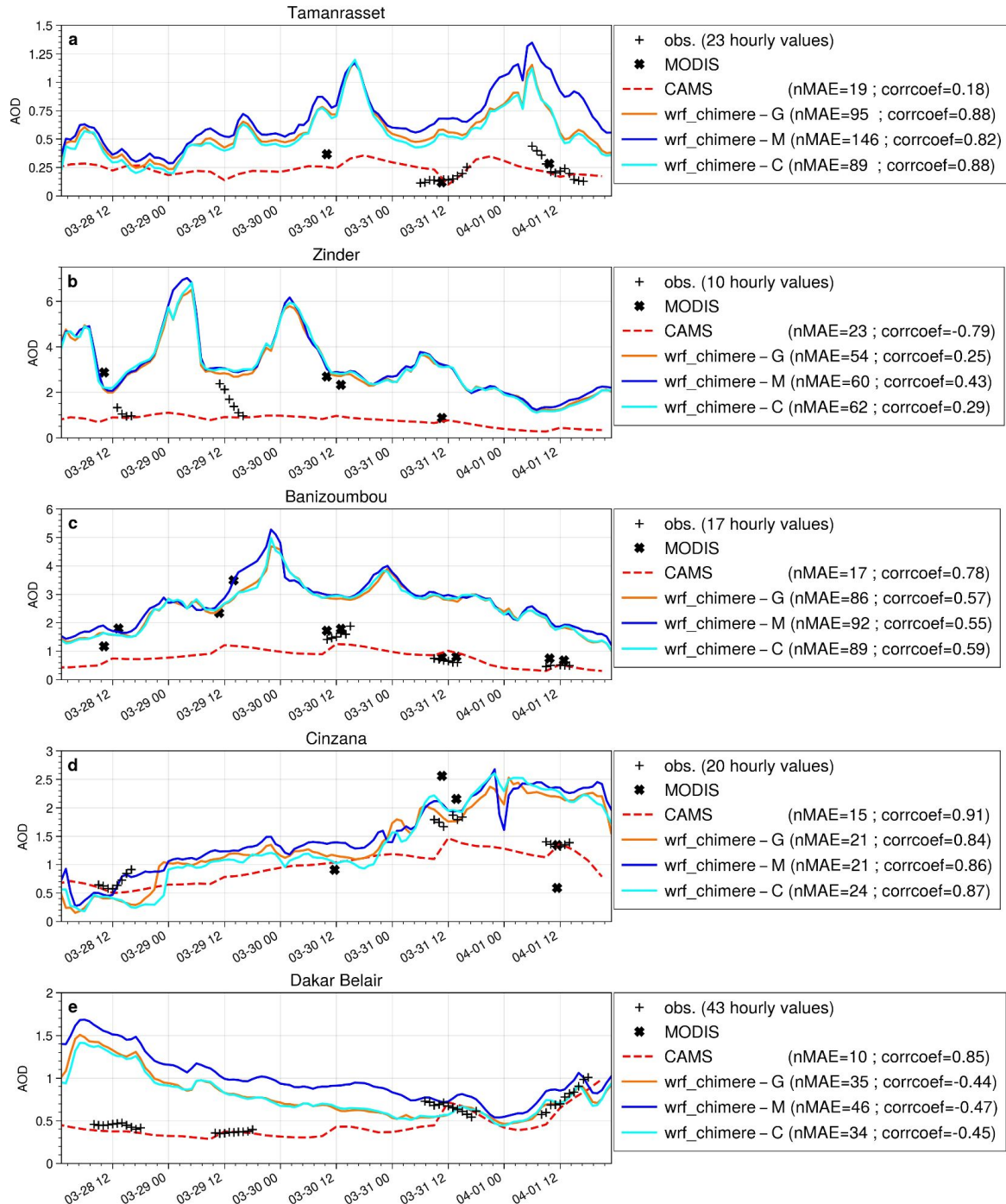
543 Furthermore, the uncertainty associated with the choice of the dust aerosol initial and
 544 boundary conditions dataset is limited. This is demonstrated by the fact that the standard
 545 deviation between the three WRF-CHIMERE simulations averaged over the period of
 546 analysis is 12% of the mean bias of those three simulations in comparison to ERA5
 547 reanalysis, and only 7% of the difference between the coupled simulations and the WRF-
 548 only simulation without dust.

549
 550 Finally, the incorporation of dust aerosol into the estimation of GHI appears to be a crucial
 551 element in this case study. However, the value of this approach is more debatable in the
 552 context of surface temperature estimation. Furthermore, the uncertainty related to the dust
 553 aerosol initial and boundary condition dataset selection is limited, particularly when

554 compared to the simulation errors, and to the differences between including dust in the
 555 simulation and not including it. The following sections will examine the simulated dust
 556 aerosol condition during the case study in order to explain the discrepancies observed in
 557 GHI and surface temperature, which are key parameters for solar production.
 558

559

3.3. Aerosol Optical Depth



560

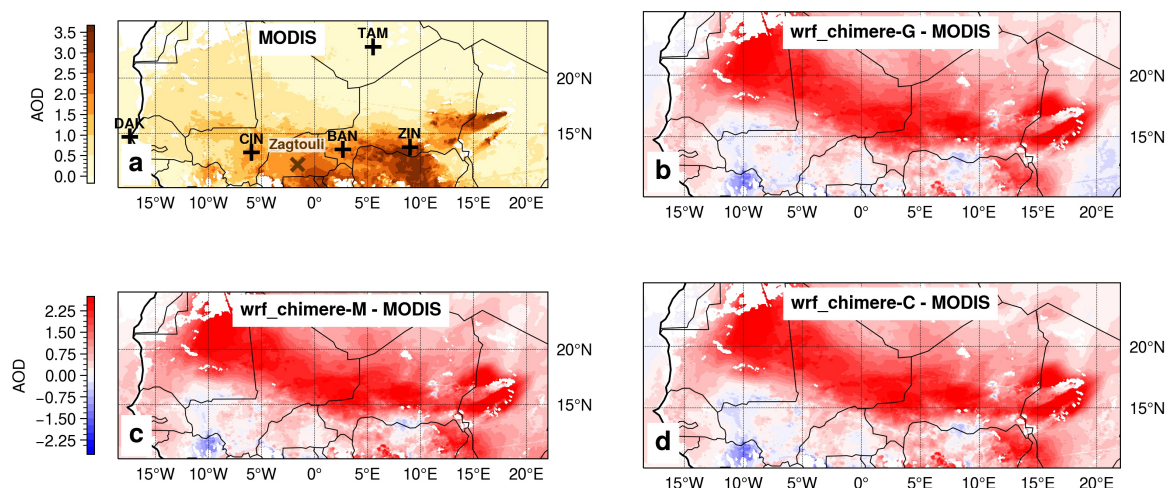
561 **Figure 6** - Local comparison of simulated AOD with AERONET in-situ measurements at 440
 562 nm for a) Tamanrasset, b) Zinder, c) Banizoumbou, d) Cinzana and e) Dakar Belair stations.
 563 *wrf_chimere-G*, *wrf_chimere-M* and *wrf_chimere-C* refer to the WRF-CHIMERE simulations
 564 using GOCART, MERRA2 and CAMS as dust aerosol initial and boundary condition dataset

565 respectively; *MODIS* and *CAMS* refer to the AOD at 440 nm from the MODIS satellite
 566 observations and the CAMS atmospheric reanalysis respectively. *nMAE* is the normalised
 567 mean absolute error in % and *corrcoef* is the Pearson correlation coefficient, both derived
 568 with AERONET measurements as the reference.

569
 570 The local evaluations presented in Figure 6 reveal an overestimation of the AOD for stations
 571 close to dust sources such as Tamanrasset (Fig. 6a), Zinder (Fig. 6b) and Banizoumbou
 572 (Fig. 6c). This overestimation is more limited with increasing distance from the dust source
 573 at Cinzana (Fig. 6d) and Dakar (Fig. 6e). The order of magnitude of the dispersion between
 574 the three simulations is small when compared to the errors of the simulation in representing
 575 the observed AOD. As a consequence, the uncertainty associated with the choice of the dust
 576 aerosol initial and boundary condition dataset is limited. Overall, the AERONET AOD
 577 measurements appear to be very scarce, particularly close to the dust aerosol sources
 578 (Zinder, Tamanrasset, Banizoumbou, Cinzana). The AOD measurements are performed by
 579 sun photometers which give recording by pointing at the sun. Thus these recordings are only
 580 available during daytime and with clear sky conditions. In some cases of intense dust
 581 plumes with very high concentration, leading to strong solar radiation absorption, the sun
 582 photometers are technically limited and cannot produce any record or, sometimes, the
 583 AERONET quality control system removes them (Mueller et al., 2015 ; Giles et al., 2019).
 584 This may be the reason for the scarcity of observations in this case study, which focuses on
 585 an intense dust event, increasing the perceived overestimation of the simulations. To
 586 compensate for this, the AOD estimates from MODIS satellite observations have been
 587 added to Figure 6 to complete the data.

588 Furthermore, the CAMS reanalysis appears to be a reliable dataset for dust AOD estimation,
 589 as it has no overestimation and has the lowest *nMAE* for all sites. Although it does not
 590 reproduce the AOD dynamics close to the dust source at Tamanrasset and Zinder, it has the
 591 highest correlation coefficient for the other sites. Nevertheless, this result should be
 592 interpreted with caution, given the limited data available for calculating the dataset
 593 evaluation metrics. More research is needed to substantiate this conclusion.

594



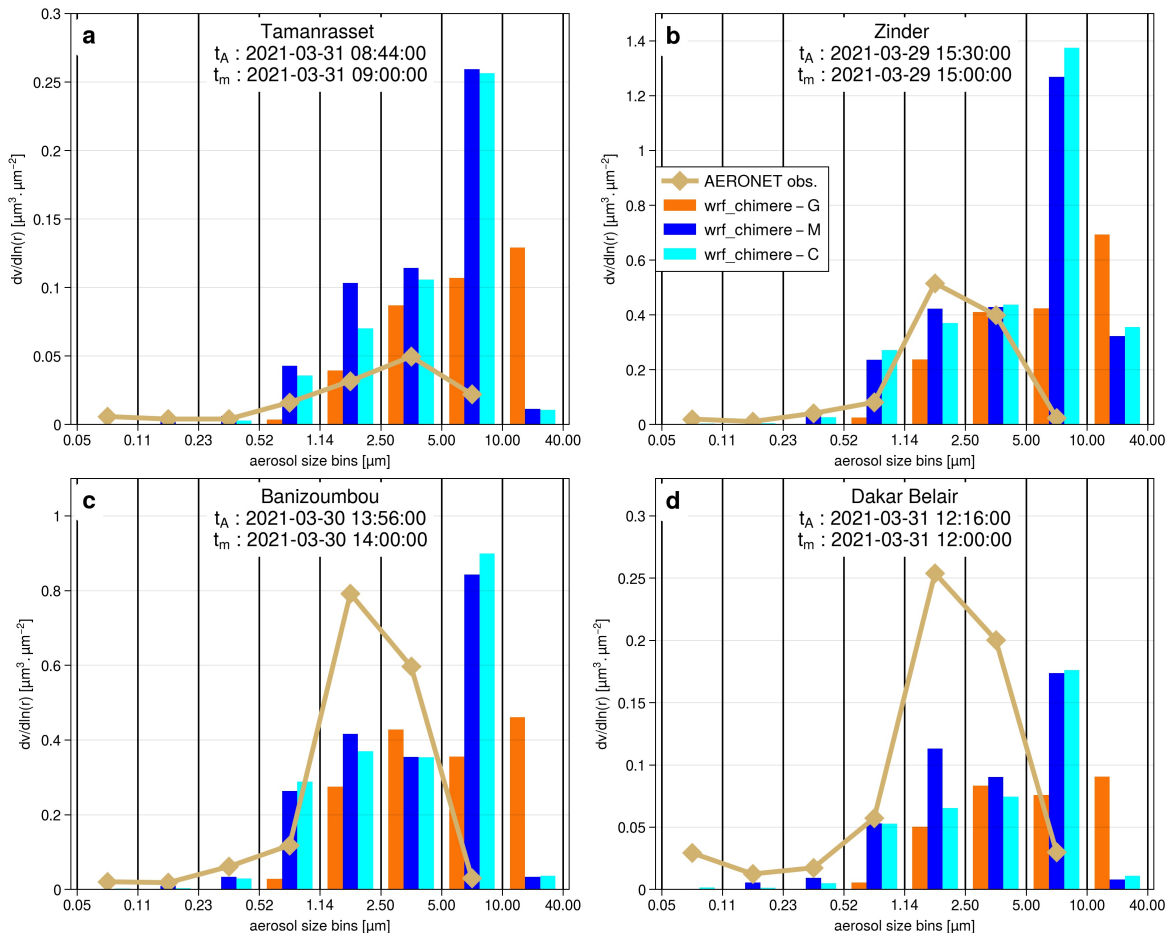
595
 596 **Figure 7** - a) Mean from March 28th-00 UTC to April 2nd-00 UTC 2021 of MODIS AOD at
 597 550 nm satellite observations; x is the Zagtouli solar farm and + corresponds to AERONET
 598 stations. For panels b, c and d, AOD at 550 nm mean differences from March 28th-00 UTC

599 to April 2nd-00 UTC 2021 between each of the WRF-CHIMERE simulations driven by
 600 GOCART, MERRA2 and CAMS, respectively, and the MODIS satellite observations.
 601

602 The AOD differences shown in Fig. 7bcd show that the simulations significantly overestimate
 603 the AOD as compared to the MODIS satellite observations, particularly in the Saharan and
 604 North Sahelian zones and in the South Atlas, with an average overestimation of +1.25
 605 between 15°N and 20°N. It is important to note that this overestimation is localised close to
 606 the desert aerosol source zones. The simulated AOD error in the Sahel zone, particularly
 607 around the Zagtouli solar power plant, is more limited with an average of +0.51 between
 608 10°N and 15°N. The mean standard deviation between the three WRF-CHIMERE
 609 simulations is only 10% of the mean error and 5% of the mean simulated AOD.
 610 Consequently the uncertainty in the AOD estimate associated with the selection of the dust
 611 aerosol initial and boundary condition dataset is small.

612 The observed overestimation of AOD by the WRF-CHIMERE simulations could be due to an
 613 overestimation of the aerosol concentration, or to an inaccurate estimation of the size
 614 distribution of the dust plume, or to excessive aerosol emissions within the domain, or to an
 615 excessive inflow of desert aerosols at the domain boundaries. These hypotheses are
 616 investigated below. Another potential explanation may also be the uncertainties in the
 617 radiative properties of the dust aerosol incorporated in the CHIMERE model, or an
 618 underestimation of the aerosol deposition flux; these aspects are not investigated here.
 619

620 3.4. Aerosol size distribution



621
 622 **Figure 8** - Aerosol volume size distribution for the AERONET station located in a)

623 Tamanrasset, b) Zinder, c) Banizoumbou and d) DakarBelair. t_A and t_m indicate the times of
624 the AERONET inversion product and the WRF-CHIMERE model respectively used for the
625 comparison. *wrf_chimere-G*, *wrf_chimere-M* and *wrf_chimere-C* refer to the WRF-CHIMERE
626 simulations using GOCART, MERRA2 and CAMS as dust aerosol initial and boundary
627 condition dataset respectively.

628

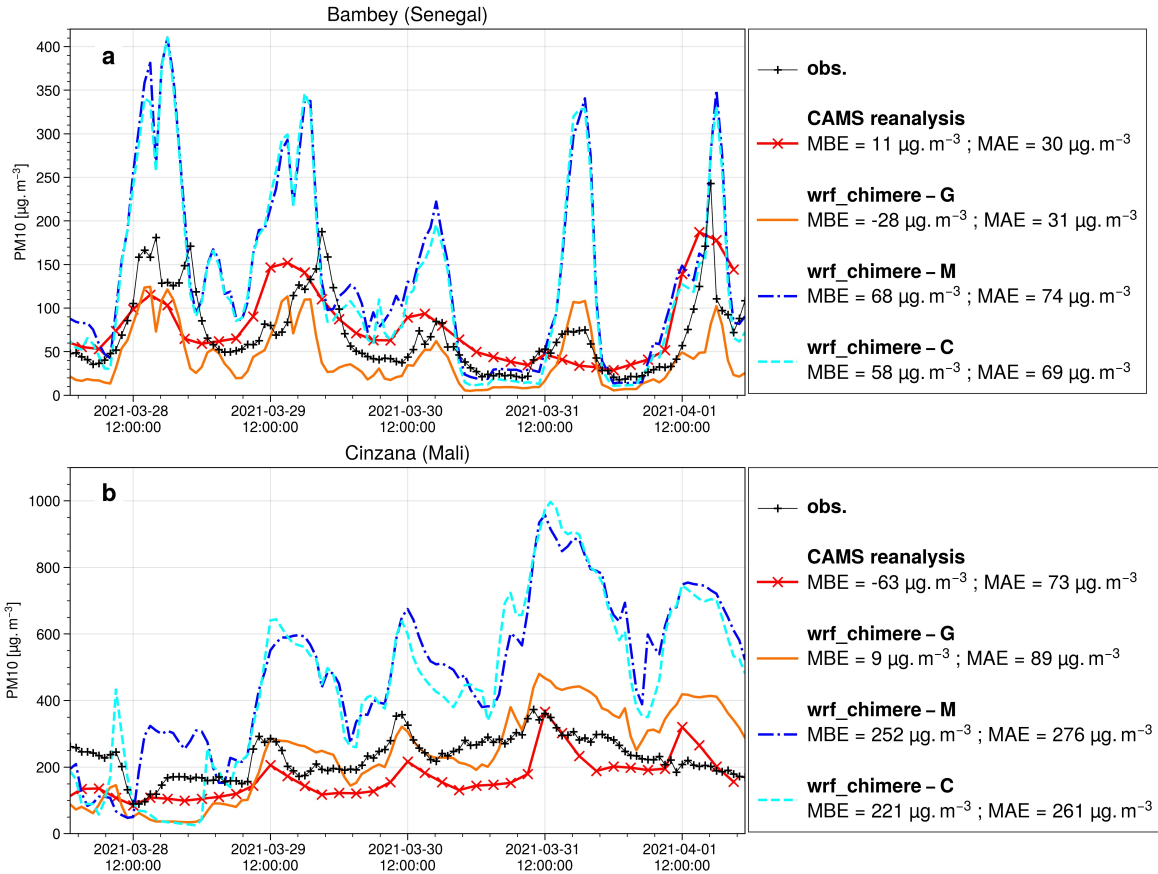
629 The evaluation of the aerosol size distribution in Fig. 8 shows that the simulations generally
630 have a dominant aerosol size mode shifted towards coarser sizes compared to the
631 AERONET inversion product. The ground-based size distribution has a strong peak between
632 1.14 μm and 5.00 μm , whereas the size distributions estimated by the WRF-CHIMERE
633 simulations peak for coarser aerosol. For the Dakar Belair station (Fig. 8d), the AERONET
634 inversion product indicates a first peak of lower intensity between 0.05 and 0.11 μm , which
635 suggests the presence of aerosols other than desert dust. These aerosols may be of
636 anthropogenic origin, given the proximity of the measurement site to the Senegalese capital.
637 When comparing the size distributions between the three simulations with different dust
638 aerosol initial and boundary condition dataset, it can be seen that the simulations driven with
639 CAMS and MERRA2 reanalysis are relatively close and well separated from the one driven
640 with the GOCART climatology. Notably, the dominant size bin in the simulation using
641 GOCART dataset is consistently the largest particles, whereas with the aerosol from
642 reanalyses, it is the aerosols between 5 μm and 10 μm . Consequently, the uncertainty
643 associated with the selection of the dust aerosol initial and boundary condition dataset is
644 high when examining the aerosol size distribution, particularly for particles exceeding 5.00
645 μm in diameter. The aforementioned uncertainties in the aerosol size distribution, which are
646 linked to the choice of the dust aerosol initial and boundary conditions dataset, may be
647 attributed to differences in the flow of desert dust entering the domain, as well as
648 uncertainties in the transfer method carried out by the CHIMERE model to match the aerosol
649 classes of these datasets to its own size distribution, described in section 2.2.3.

650 As a result, the shift in the WRF-CHIMERE size distribution towards coarser particles
651 compared to AERONET observations would result in a simulated AOD smaller than
652 AERONET measurements. However, the opposite is observed (section 3.3). This suggests a
653 positive bias in the simulated aerosol concentration, which would explain the positive bias in
654 the AOD, while the coarser size distribution would tend to compensate.

655

656

3.5. Aerosol concentrations

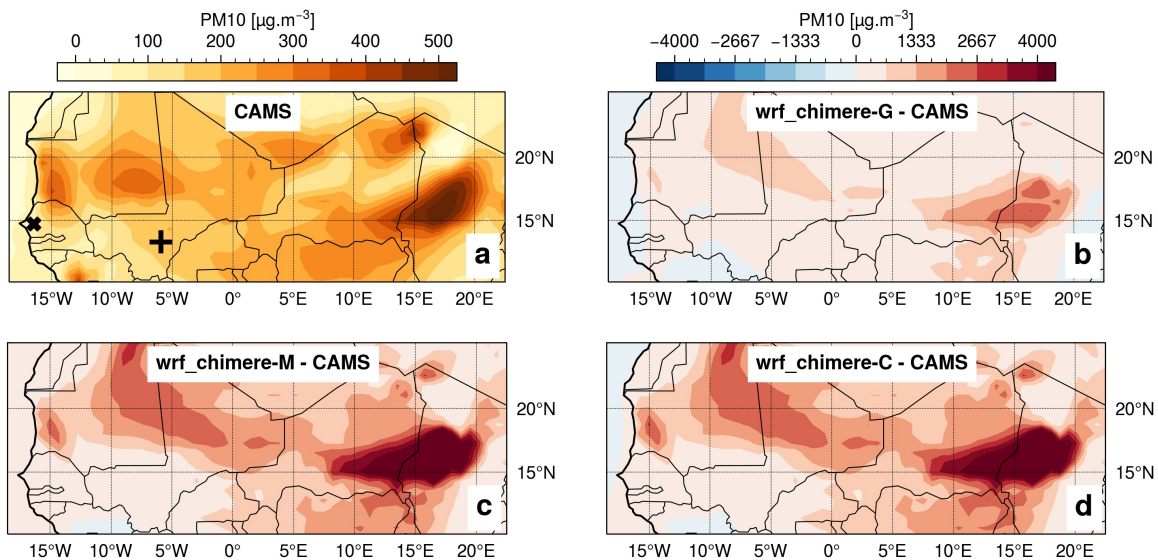


657
 658 **Figure 9** - Local comparison of CAMS reanalysis and simulated PM₁₀ surface concentrations
 659 with INDAAF network observations for a) Cinzana and b) Bambeey stations. *wrf_chimere-G*,
 660 *wrf_chimere-M* and *wrf_chimere-C* refer to the WRF-CHIMERE simulations using GOCART,
 661 MERRA2 and CAMS as dust aerosol initial and boundary condition dataset respectively.
 662 MBE is the mean bias error and MAE refers to the mean absolute error.

663
 664 The three simulations properly capture the dynamics of the PM₁₀ surface concentration with
 665 respect to the INDAAF ground measurement (Fig. 9) as correlation coefficients are around
 666 0.6 at Cinzana and close to 0.7 at Bambeey. The WRF-CHIMERE simulations driven with
 667 MERRA2 and CAMS dust aerosol datasets overestimate the surface PM₁₀ concentration
 668 peaks for Bambeey (Fig. 9a) and Cinzana (Fig. 9b), with high positive bias values of around
 669 63 g.m⁻³ at Bambeey and 247 g.m⁻³ at Cinzana. The latter station is closer to the dust
 670 aerosol sources. In contrast, the simulation using the GOCART dust aerosol dataset
 671 demonstrates superior performance in representing this variable, with an MAE that is
 672 approximately 60% and 70% lower than the two other simulations at Bambeey and Cinzana,
 673 respectively.

674 Furthermore, the uncertainty associated with the selection of initial and boundary condition
 675 dataset for dust aerosols is of a comparable magnitude to the simulation errors observed for
 676 surface PM₁₀ concentrations. Section 3.4 partly explains these discrepancies in surface PM₁₀
 677 concentration estimates between the simulation driven with the GOCART climatology and
 678 those driven with CAMS or MERRA2 reanalysis in terms of aerosol size distribution. These
 679 differences may also be attributed to variations in the size distribution of dust aerosol
 680 emissions or in the inflow of dust into the simulation domain and its aerosol size distribution.

681 Furthermore, Fig. 9 indicates that the CAMS reanalysis provides reliable estimates of
 682 surface PM₁₀ concentration, as evidenced by the fact it has the lowest MAE values.
 683 However, the Bambey and Cinzana ground measurements, which are the only two available
 684 for the case study, are situated at a considerable distance from the dust sources, limiting our
 685 ability to assess the accuracy of the CAMS reanalysis in capturing the dust event. Moreover,
 686 the CAMS reanalysis exhibits a negative bias at Cinzana, which is the closest site to the dust
 687 sources.
 688

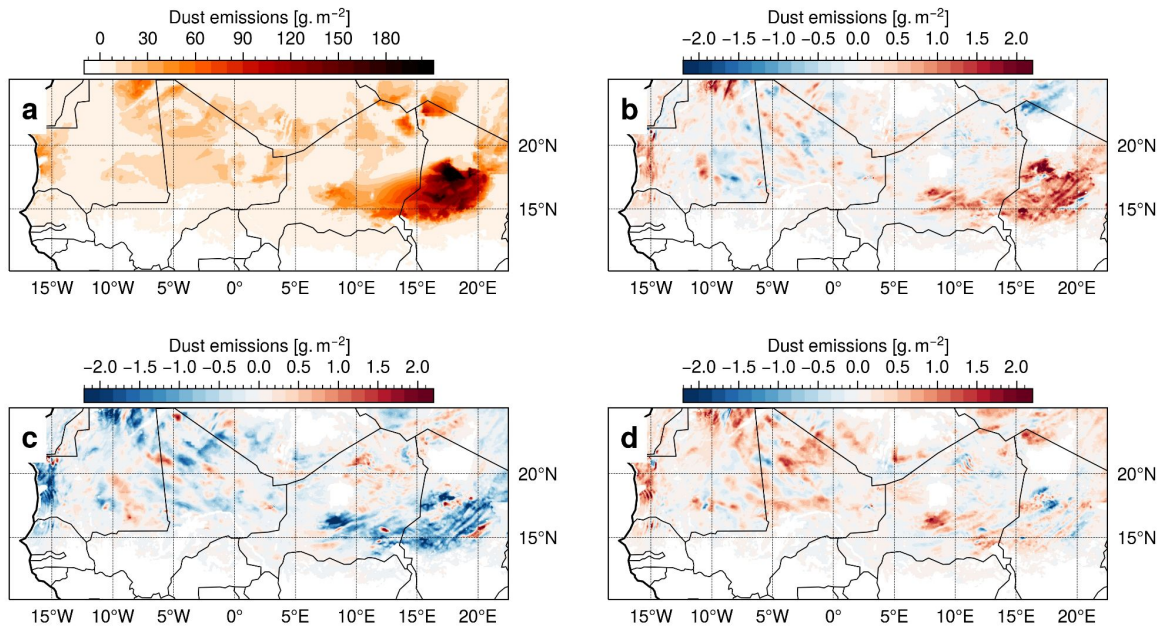


689 **Figure 10** - a) Mean from March 28th-00 UTC to April 2nd-00 UTC 2021 of CAMS reanalysis
 690 PM₁₀ surface concentration; x refers to the Bambey and + corresponds to Cinzana INDAAF
 691 stations. For panels b, c and d, PM₁₀ surface concentration mean differences from March
 692 28th-00 UTC to April 2nd-00 UTC 2021 between each of the WRF-CHIMERE simulations
 693 driven by GOCART, MERRA2 and CAMS, respectively, and the CAMS reanalysis.
 694

695
 696 Figure 10 illustrates an overestimation of the PM₁₀ concentrations as compared to the CAMS
 697 reanalysis. This is particularly evident in dust source areas such as the Bodele Depression.
 698 The WRF-CHIMERE simulation driven with the GOCART dataset is the closest to the CAMS
 699 reanalysis, with a mean estimate 3.6 times higher. However, this ratio reaches 8.6 for the
 700 simulations driven with the CAMS and MERRA2 reanalysis dataset.

701 The mean standard deviation between the three WRF-CHIMERE simulations is 35% of their
 702 mean PM₁₀ surface concentration estimate. Consequently the uncertainty in the estimation of
 703 dust PM₁₀ surface concentration associated with the selection of the dust aerosol initial and
 704 boundary condition dataset is significant. The discrepancies between the simulation using
 705 the GOCART climatology and the two other ones using CAMS or MERRA2 reanalysis can
 706 be partly explained by the differences in the simulated aerosol size distribution, as shown in
 707 section 3.4.

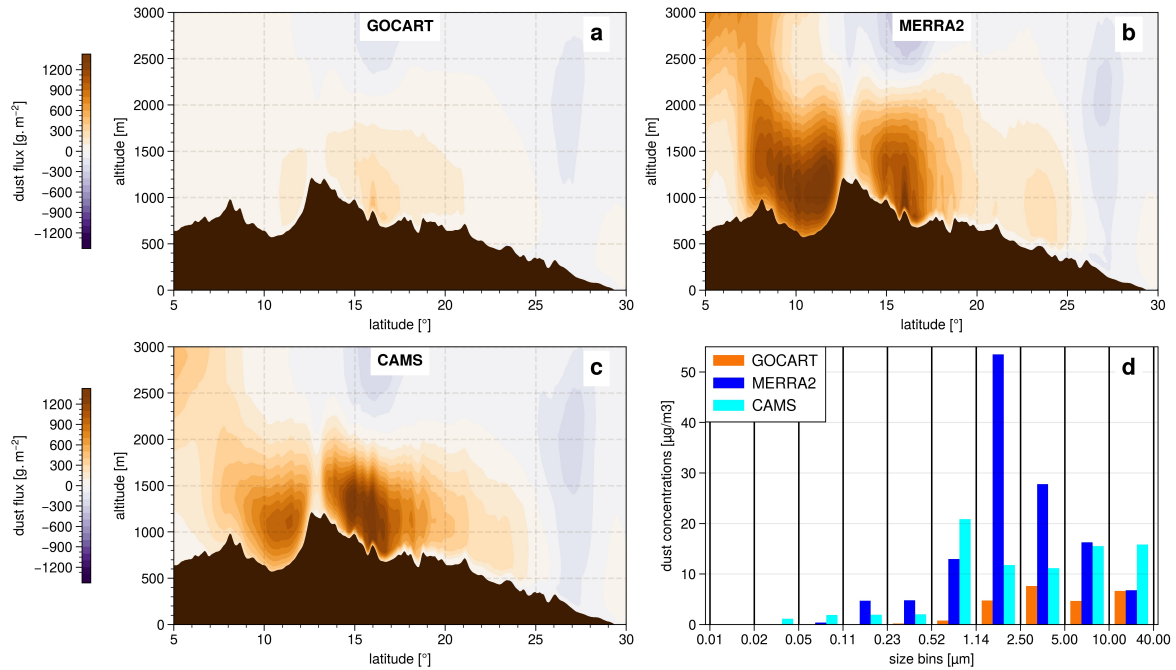
708
 709 **3.6. Dust emissions**



710
 711 **Figure 11** - a) Total dust emissions flux from March 28th-00 UTC to April 2nd-00 UTC 2021,
 712 averaged between the three WRF-CHIMERE simulations. For panels b, c and d, total dust
 713 emissions individual differences between each of the WRF-CHIMERE simulations driven by
 714 GOCART, MERRA2 and CAMS, respectively, and the mean of the three WRF-CHIMERE
 715 simulations.

716
 717 In terms of dust emissions (Fig. 11), the Bodele Depression is, as expected, identified as
 718 the primary dust source area, with emissions reaching up to 244 g/m^2 . The differences of the
 719 simulations with each of the three dust aerosol initial and boundary conditions dataset,
 720 relative to their mean, exhibit highest values in the source zones located at the Bodele
 721 Depression and the South Atlas. Nevertheless, it is worth noting that there is a factor of 100
 722 in between the emissions in the Bodele area (approximately 200 g/m^2) and the observed
 723 differences between the three simulations. Consequently, the uncertainties in dust emissions
 724 resulting from the choice of the dust aerosol initial and boundary conditions dataset can be
 725 considered negligible. As emissions are primarily influenced by surface wind, it can be
 726 inferred that the uncertainty generated by the dust aerosol driving dataset on the surface
 727 wind is negligible too, which is confirmed by Fig. S4. Additionally, the size distributions of the
 728 aerosols emitted during the case study are found to be identical (not shown). Therefore, the
 729 differences in dust surface concentration and dust aerosol size distribution may be partly
 730 attributed to the dust flows at the boundaries of the domain and are not linked to differences
 731 in simulated dust emissions within the domain. However, there is no observational data
 732 available to enable a quantitative evaluation of the accuracy of the emissions computed
 733 within the WRF-CHIMERE simulations.

734
 735 **3.7. Dust boundary flux**



736
 737 **Figure 12** - Cumul of the dust flux at the eastern boundary of the simulation from March
 738 28th-00 UTC to April 2nd-00 UTC 2021 for the WRF-CHIMERE simulation with a) GOCART,
 739 b) MERRA2 and c) CAMS as dust aerosol initial and boundary conditions dataset; d) Dust
 740 size distribution at the eastern boundary limit average during the case study period, from the
 741 surface to 200hPa and over latitude. In panel abc, the dust flux is derived as the product
 742 between the dust aerosol concentration and the zonal wind, and positive values of the dust
 743 flow indicate a flow entering the simulation domain.

744
 745 As shown in Fig. 1b, the dust event is associated with a strong Harmattan flow,
 746 characterised by a northeasterly flow in the lower layer. It is thus interesting to quantify the
 747 dust inflow associated with each of the dust aerosol initial and boundary conditions dataset
 748 for the eastern domain boundary. The lowest dust flux is observed with GOCART (Fig. 12a),
 749 with a maximum of approximately 480 g/m^2 . In contrast, MERRA2 and CAMS (Fig. 14 b
 750 and c respectively) exhibit higher dust fluxes, with maximum values of around 1650 g/m^2 .
 751 The maximum flow is around 10°N for MERRA2, while for CAMS, it is closer to 16°N . Given
 752 that GOCART is a climatology, it is reasonable to expect a lower dust flux compared to the
 753 CAMS and MERRA2 reanalyses, which are real case simulations incorporating data
 754 assimilation of AOD. This is particularly true for the presented case study, which involves an
 755 intense dust event associated with a Harmattan flow.

756 There are also significant differences in both quantity and distribution by aerosol size bin
 757 (Fig. 12d). MERRA2 exhibits a strong dominant mode for the class between $1.14 \mu\text{m}$ and
 758 $2.50 \mu\text{m}$, while CAMS shows significant values from $0.52 \mu\text{m}$ to $40 \mu\text{m}$, with a maximum for
 759 the size class between $0.52 \mu\text{m}$ and $1.14 \mu\text{m}$. Finally, the GOCART model displays a lower
 760 variability between $1.14 \mu\text{m}$ and $40.00 \mu\text{m}$, with the maximum occurring for the size class
 761 between $2.55 \mu\text{m}$ and $5.00 \mu\text{m}$.

762 The eastern dust fluxes at the boundary significantly vary depending on the dataset used as
 763 dust aerosol initial and boundary conditions, both in terms of quantity and size distribution.
 764 The reanalysis dataset, CAMS and MERRA2, are expected to provide a more accurate
 765 representation of dust flux in terms of quantity as they are real case simulations assimilating

766 observational data in their calculations, as compared to GOCART which is a climatology.
767 However, GOCART provides a more comprehensive description of aerosol size distribution
768 with seven classes, in comparison to CAMS, which has only three classes but proposes a
769 higher horizontal resolution. While GOCART considers the effect of aerosol size to be
770 essential, CAMS assumes the horizontal resolution to be a key parameter. MERRA2 is the
771 most comprehensive of the three datasets, with the highest horizontal resolution, and an
772 aerosol size distribution that is close to the GOCART one with five classes.
773 As a result, and in consideration of the negligible uncertainty in dust emissions within the
774 simulation domain related to the choice of the dataset for dust aerosol initial and boundary
775 conditions (see 3.6), these differences in eastern dust fluxes appear to account for the
776 uncertainties of the simulated surface dust concentrations (see 3.5) and dust aerosol size
777 distribution (see 3.4).

778

779 **3.8. Discussions**

780 The evaluation of the simulated GHI at the Zagtouli solar power plant and the Banizoumbou
781 site (Fig. 2) indicates a significant enhancement in surface solar irradiance estimation when
782 WRF is coupled with CHIMERE. Specifically, the local MAE is reduced by approximately
783 75%. This confirms the relevance of incorporating the dust radiative effect with a coupling
784 approach, in comparison with the operational forecasts currently employed based on
785 meteorological models alone. During the dry season, dust events similar to the one
786 presented here, with emissions at Bodele and then transport of the plume westwards, are
787 common. This work therefore calls for forecasters in the photovoltaic sector to better account
788 for the desert dust cycle in their forecast products. This local evaluation also highlights the
789 potential benefits of using a regional model rather than a global product, as the WRF-
790 CHIMERE simulations outperform the CAMS gridded solar radiation product with an average
791 MAE reduced by approximately 38% at the Zagtouli solar farm and by 70% at the
792 Banizoumbou site, which is closer to dust sources. These discrepancies are corroborated by
793 the regional comparison presented in Figure 3, which reveals that the mean WRF-CHIMERE
794 GHI estimate is 5% lower than the CAMS solar radiation dataset. Additionally, the latter does
795 not exhibit a geographical pattern with lower GHI estimation along the dust plume trajectory,
796 in contrast to the WRF-CHIMERE simulations. These results confirm those from Sawadogo
797 et al. (2023) who recently showed that the CAMS reanalysis have low performances in
798 estimating solar irradiance during high AOD episodes like the one studied here.
799 Furthermore, the comparison reveals that incorporating dust in the simulation reduces
800 surface solar irradiance by 18% in this case study. This reduction is notably higher but
801 remains within the same order of magnitude as previous studies that integrated dust aerosol
802 information for solar estimation. For example, Masoom et al. (2021) in India and Mostamandi
803 et al. (2023) in the Arabian Peninsula reported GHI reductions due to dust of approximately
804 5-10%. This discrepancy underscores the potential variability of the dust impact on solar
805 irradiance depending on the method used to account for dust effects in the simulations. In
806 light of the anticipated expansion of PV production in West Africa, this point underscores the
807 potential consequences of such dust events if they are not accurately predicted.

808

809 The evaluation of local surface temperature (Fig. 4) reveals contrasting results regarding the
810 effectiveness of the coupled approach. It demonstrates an average local MAE reduction of
811 approximately 10% compared to the WRF-only simulation. However, the main differences
812 occur mainly at night, when no photovoltaic is produced, as previously observed by Yue et
813 al. (2010) and Briant et al. (2017). It can be attributed to the opposing radiative forcing

814 effects of dust aerosols across different wavelength ranges. In the case of longwave, which
815 corresponds to terrestrial radiation, the presence of dust aerosols has a warming effect.
816 Conversely, for shortwave, which corresponds to solar radiation, the presence of dust
817 aerosols induces a cooling effect. Consequently, during night-time when solely terrestrial
818 radiation is present, there is an increase in surface temperature. During day-time a
819 competition between the warming effect of terrestrial radiation and the cooling effect of solar
820 radiation ensues. The net impact is a decrease in surface temperature, indicating that the
821 effect of solar radiation dominates, with the cooling effect exceeding the warming effect
822 (Sokolik and Toon, 1999).

823 The regional evaluation in Fig. 5 confirms these contrasting results and indicates a reduction
824 of regional MAE by about 14% with the coupling rather than WRF alone. The overestimation
825 of surface temperature in dusty areas with the coupling, not present in the WRF only
826 simulation, reveals the dominant aerosol warming effect during night time as compared to
827 the cooling effect during daytime. These results align with those of Briant et al. (2017), who
828 estimated dust-induced warming of up to +5°C during nighttime and cooling of approximately
829 -1°C during daytime in a 2012 dust event in West Africa. These statements strongly depend
830 on the accuracy of the ERA5 reanalysis which serves as reference. ERA5 integrates data
831 assimilation of temperature and incorporates aerosol radiative effects through prescribed
832 monthly climatologies from the GOCART model, but does not dynamically simulate aerosols.
833 Due to the limited ground measurements in the Saharan region to constrain the reanalysis,
834 and to the significant biases that can come when considering a coarse climatology for the
835 radiative effects of aerosols to represent an intense dust event, it is possible that ERA5
836 underestimates the aerosol effect in dusty areas.

837

838 Nevertheless, despite the improvements demonstrated in solar irradiance and surface
839 temperature estimation, the WRF-CHIMERE simulations exhibit a notable positive bias in
840 terms of AOD, as evidenced by the local and regional evaluations presented in Figs. 6 and
841 7. This overestimation cannot be attributed solely to differences in aerosol concentrations, as
842 the simulations yield markedly disparate surface concentrations of PM10, depending on the
843 dust aerosol initial and boundary condition dataset chosen (Fig. 10), while this discrepancies
844 do not appear in the AOD estimates. However, the results from Yahi et al. (2013) and Léon
845 et al. (2020) emphasized the importance of considering dust plume height when linking
846 surface PM10 concentrations to AOD. Therefore, differences in the vertical distribution of the
847 dust plume, not evaluated in this study due to the lack of quantitative observational data,
848 could account for part of the observed discrepancies between simulated AODs and surface
849 PM10 concentrations. This excess of aerosol load may be attributed to an overestimation of
850 emissions within the domain, but this cannot be verified as there is not any such
851 measurement. The incoming flux of dust in the domain plays a minor role as shown in Fig.
852 12 where the flux significantly also varies depending on the dust aerosol initial and boundary
853 condition dataset employed, while these differences are not any more present in the
854 simulated AOD estimates. Additionally, the underestimation of aerosol deposition, by
855 sedimentation (not studied in this research) could be at the origin of the overestimation of the
856 simulated dust loads. Finally, another potential explanation for these AOD biases may be the
857 inaccuracies in the dust radiative properties incorporated in the CHIMERE model calculation
858 (see Table S1 and S2). These depend on the mineralogical composition of the desert dust
859 particles emitted, which are considered uniform in this work. The radiative properties of
860 aerosols also depend on their granulometry. In the CHIMERE model, dust aerosols are
861 treated as spherical particles in the calculation of their radiative properties using Mie theory,

862 which introduces biases. Adbiyi et al. (2023) showed that ellipsoidal dust particles have a
863 slightly higher mass extinction efficiency compared to spherical particles. As a result,
864 accounting for ellipsoidal dust aerosols would lead to a slight increase in AOD associated
865 with a small decrease in GHI. This study further indicates that dust particles with radii
866 smaller than 20.0 μm are the primary contributors to dust AOD for shortwave radiation, with
867 the contribution from larger particles being an order of magnitude lower. Therefore, including
868 particles larger than 40.0 μm in the CHIMERE model would not significantly affect AOD and
869 GHI estimates. This is corroborated by Mostamandi et al. (2023), who demonstrated that
870 dust particles with radii smaller than 3 μm are primarily responsible for the reduction in solar
871 irradiance, while particles larger than 10 μm mainly contribute to dust deposition, which was
872 not examined in this study.

873

874 The uncertainty associated with the choice of the large scale dust aerosol initial and
875 boundary condition dataset is very low when considering the variables of interest for solar
876 production, namely GHI and surface temperature (Fig. 3 and 5). This uncertainty is also low
877 compared to the performance of simulations for AOD estimation (Fig. 7). This result is similar
878 when examining dust emissions within the domain, which are nearly identical for the three
879 coupled simulations (Fig. 11). This can be explained by the fact that dust emissions depend
880 on the cube of surface wind speed (Marticorena and Bergametti, 1995) which present no
881 significant signature of the selection of the dust aerosol initial and boundary conditions (Fig.
882 S4). The aerosols emitted within the chosen domain are much greater than those entering,
883 as the domain accounts for the main source zones. This is why the simulations are not that
884 sensitive to dust aerosol large-scale dataset employed. The results regarding the uncertainty
885 associated with the choice of the dust aerosol initial and boundary condition dataset differs
886 when examining various elements of the dust life cycle. Indeed, aerosol size distributions
887 vary significantly between the simulation driven with GOCART on one hand, and simulations
888 driven with CAMS and MERRA2 on the other hand. GOCART climatology over-represents
889 aerosols larger than 10 μm compared to the CAMS and MERRA2 reanalyses. These
890 differences partially account for the significant deviation in surface PM_{10} concentration
891 estimates (Fig. 10), indicating that reanalysis-type datasets result in much higher values, up
892 to 3 times higher, compared to climatological-type data which is closer to ground
893 observations. The dust flux entering the domain may also partly explain these differences. In
894 fact, this flux is very low with GOCART, with values up to 3.5 times lower than CAMS and
895 MERRA2 (Fig. 12). The size distribution of this incoming aerosol flux is also a determining
896 factor.

897

898 **4. Conclusion and perspectives**

899 This study aims to evaluate the ability of the WRF-CHIMERE coupling to simulate GHI
900 during a typical dust event in the dry season in West Africa. This event is characterised by a
901 Harmattan flux associated with significant desert dust emissions over the Bodele
902 Depression, with the dust plume subsequently transported westward. This work
903 demonstrates the utility of coupling a meteorological model with a desert aerosol life cycle
904 model to represent such events, particularly for improving solar forecasts. Indeed, GHI
905 estimations are markedly enhanced with this approach compared to using a meteorological
906 model alone with a 75% reduction of local MAE. Nevertheless, the performance of the WRF-
907 CHIMERE simulations in representing the aerosol load of this event is more controversial.
908 There is an overall overestimation of AOD and PM_{10} surface concentration by the coupled
909 model in the North Sahelian-Saharan zone.

910 This work also aims at investigating whether the performance of the simulations can be
911 improved by changing the dust aerosol initial and boundary condition dataset, and to
912 estimate the uncertainty associated with this choice. The results show that this selection has
913 almost no influence on the estimation of the solar irradiance, surface temperature and AOD.
914 On the contrary, the choice of the dust aerosol initial and boundary condition dataset has a
915 significant impact on the surface PM₁₀ concentration and the aerosol size distribution.

916

917 This work outlines new research perspectives. Firstly, we observe the difficulty of evaluating
918 simulations in West Africa due to the scarcity of available observations. Establishing a
919 denser measurement network or conducting observation campaigns, particularly for GHI,
920 would help research on solar estimation and forecasting in this region. Additionally, the
921 WRF-CHIMERE simulations demonstrate significant biases in terms of AOD and PM₁₀
922 surface concentration which are not fully explained here. One potential explanation for this is
923 an overestimation of dust emission, for which no evaluation is possible. Furthermore,
924 studying aerosol deposition (not conducted in this work) would complement the study of the
925 desert aerosol life cycle. On the one hand, an underestimation of deposition might be a
926 contributing factor to the overestimation of the simulated aerosol load. On the other hand,
927 dust deposition on solar panels affects solar production by masking the available solar
928 irradiance (soiling effect), and this should be taken into account in forecasting systems to
929 conduct optimised cleaning operations. A further limitation of this study is the use of the
930 WRF meteorological model for the coupling with CHIMERE, rather than the WRF-Solar
931 model (Jimenez et al., 2016), which is an enhanced version of WRF dedicated to solar
932 forecasting. Indeed, WRF-Solar incorporates enhanced algorithms for the computation of
933 solar irradiance, accounting for the direct and indirect effects of aerosols and employing an
934 advanced solar tracking algorithm. This makes it the appropriate version of WRF to use for
935 solar energy research. However, no coupling between WRF-Solar and CHIMERE has yet
936 been implemented, representing an important perspective to expend this work. Finally, the
937 study focuses on a typical dust event during the dry season, presenting essentially aerosol-
938 radiation interaction. It could be beneficial to test such simulation configuration for more
939 complex cases involving cloud presence. Indeed, the interaction between aerosols and
940 clouds have a significant impact on solar forecasting by increasing albedo, extending cloud
941 lifespan, and promoting cloud formation through increased condensation nucleus
942 concentration (indirect aerosol effects).

943

944 **Code and data availability**

945 WRF namelist configuration files, CHIMERE parameter files, Python codes exploited in this
946 study and GOCART climatology data can be found on the following Zenodo repository:
947 <https://zenodo.org/records/10808476>

948 ERA5 data can be found on the Copernicus Climate Data Store service :
949 <https://cds.climate.copernicus.eu/cdsapp#!/home>

950 CAMS data were downloaded on the Copernicus Atmosphere Data Store service :
951 <https://ads.atmosphere.copernicus.eu/cdsapp#!/home>

952 MERRA2 data can be found on the dedicated platform from NASA :
953 <https://goldsmr5.gesdisc.eosdis.nasa.gov/data/MERRA2/>

954 Data from AMMA ground measurements stations can be accessed from the dedicated
955 website : <https://amma-catch.osug.fr/-jeux-de-donnees->

956 INDAAF web page allows access to the data : <https://indaaf.obs-mip.fr/catalogue/>

957 AERONET data measurements and inversion products are available through the following
958 link: <https://aeronet.gsfc.nasa.gov/>

959 The MODIS satellite observations are available on the “Level-1 and Atmosphere Archive &
960 Distribution System Distributed Active Archive Center” platform from NASA :
961 <https://ladsweb.modaps.eosdis.nasa.gov/>

962

963 **Author contributions**

964 LC, SA, CL conceptualised the study. LC performed the simulations, the analysis and the
965 editions of the figures. LC, SA, CL, GB, BM, GS, CB, RL and JT discussed the results. LC
966 wrote the paper

967

968 **Competing interest**

969 The contact author has declared that none of the authors has any competing interests.

970

971 **Acknowledgment**

972 This work has been supported by the NETWAT project (ANR-22-CE03-0011) operated by
973 the French National Research Agency. To conduct the simulations, this study has benefited
974 from access to the IPSL-SU (SPIRIT) cluster within the IPSL Mesocentre ESPRI facility,
975 supported by the CNRS, UPMC, Labex L-IPSL, CNES and Ecole Polytechnique. The
976 authors want to thank the WRF and CHIMERE developers for giving free access to their
977 model. We thank the National Aeronautics and Space Agency for the availability of the
978 MODIS and the MERRA2 data, the European Center for Medium-Range Weather Forecasts
979 for the availability of the CAMS and ERA5 data and the investigators and staff who maintain
980 and provide the AERONET, the INDAAF and the AMMA-CATCH observational data. Finally,
981 we thank the Sonabel company for their contribution.

982 During the preparation of this work the authors used DeepL Write (DeepL SE) in order to
983 improve language and readability. After using this tool/service, the authors reviewed and
984 edited the content as needed and take full responsibility for the content of the publication.

985

986 **References**

987 Adebisi, A., Kok, J.F., Murray, B.J., Ryder, C.L., Stuut, J.-B.W., Kahn, R.A., Knippertz,
988 P., Formenti, P., Mahowald, N.M., Pérez García-Pando, C., Klose, M., Ansmann,
989 A., Samset, B.H., Ito, A., Balkanski, Y., Di Biagio, C., Romanias, M.N., Huang, Y.,
990 Meng, J., 2023. A review of coarse mineral dust in the Earth system. *Aeolian*
991 *Research* 60, 100849. <https://doi.org/10.1016/j.aeolia.2022.100849>

992 Africa Energy Outlook 2022, n.d.

993 Aidara, M.C., Fam, P.A., Danso, D.K., Mortey, E.M., Mbaye, A., Ndiaye, M.L.,
994 Bonkaney, A.L., Adamou, R., Anquetin, S., Diedhiou, A., 2023. Contribution to the
995 building of a weather information service for solar panel cleaning operations at
996 Diass plant (Senegal, Western Sahel). *Open Geosciences* 15.
997 <https://doi.org/10.1515/geo-2022-0449>

998 Alfaro, S.C., Gomes, L., 2001. Modeling mineral aerosol production by wind erosion:
999 Emission intensities and aerosol size distributions in source areas. *Journal of*
1000 *Geophysical Research: Atmospheres* 106, 18075–18084.
1001 <https://doi.org/10.1029/2000JD900339>

1002 AMMA-CATCH (2005): Meteorological dataset (including radiative budget and soil
1003 variables), within the Niamey square degree site (16 000 km²), Niger. IRD, CNRS-
1004 INSU, OSUG, OMP, OREME. [doi:10.17178/AMMA-CATCH.AL.Met_Nc](https://doi.org/10.17178/AMMA-CATCH.AL.Met_Nc)

1005 Arakawa, A., 2004. The Cumulus Parameterization Problem: Past, Present, and Future.
1006 Journal of Climate 17, 2493–2525. [https://doi.org/10.1175/1520-
1007 0442\(2004\)017<2493:RATCPP>2.0.CO;2](https://doi.org/10.1175/1520-0442(2004)017<2493:RATCPP>2.0.CO;2)

1008 Bergametti, G., Marticorena, B., Rajot, J.L., Chatenet, B., Féron, A., Gaimoz, C., Siour,
1009 G., Coulibaly, M., Koné, I., Maman, A., Zakou, A., 2017. Dust Uplift Potential in the
1010 Central Sahel: An Analysis Based on 10 years of Meteorological Measurements at
1011 High Temporal Resolution. Journal of Geophysical Research: Atmospheres 122,
1012 12,433-12,448. <https://doi.org/10.1002/2017JD027471>

1013 Bian, H., Prather, M.J., n.d. Fast-J2: Accurate Simulation of Stratospheric Photolysis in
1014 Global Chemical Models.

1015 Bou Karam, D., Flamant, C., Tulet, P., Chaboureau, J.-P., Dabas, A., Todd, M.C., 2009.
1016 Estimate of Sahelian dust emissions in the intertropical discontinuity region of the
1017 West African Monsoon. Journal of Geophysical Research: Atmospheres 114.
1018 <https://doi.org/10.1029/2008JD011444>

1019 Briant, R., Tuccella, P., Deroubaix, A., Khvorostyanov, D., Menut, L., Mailler, S.,
1020 Turquety, S., 2017. Aerosol–radiation interaction modelling using online coupling
1021 between the WRF 3.7.1 meteorological model and the CHIMERE 2016 chemistry-
1022 transport model, through the OASIS3-MCT coupler. Geoscientific Model
1023 Development 10, 927–944. <https://doi.org/10.5194/gmd-10-927-2017>

1024 Clauzel, L., Anquetin, S., Lavaysse, C., Tremoy, G., Raynaud, D., 2024. West African
1025 operational daily solar forecast errors and their link with meteorological conditions.
1026 Renewable Energy 224, 120101. <https://doi.org/10.1016/j.renene.2024.120101>

1027 d’Almeida, G.A., 1986. A Model for Saharan Dust Transport. Journal of Applied
1028 Meteorology and Climatology 25, 903–916. [https://doi.org/10.1175/1520-
1029 0450\(1986\)025<0903:AMFSDT>2.0.CO;2](https://doi.org/10.1175/1520-0450(1986)025<0903:AMFSDT>2.0.CO;2)

1030 Dajuma, A., Yahaya, S., Touré, S., Diedhiou, A., Adamou, R., Konaré, A., Sido, M.,
1031 Golba, M., 2016. Sensitivity of Solar Photovoltaic Panel Efficiency to Weather and
1032 Dust over West Africa: Comparative Experimental Study between Niamey (Niger)
1033 and Abidjan (Côte d’Ivoire). Computational Water, Energy, and Environmental
1034 Engineering 5, 123–147. <https://doi.org/10.4236/cweee.2016.54012>

1035 Diabaté, L., Blanc, P., Wald, L., 2004. Solar radiation climate in Africa. Solar Energy 76,
1036 733–744.

1037 Diop, D., Drame, M.S., Diallo, M., Malec, D., Mary, D., Guillot, P., 2020. Modelling of
1038 Photovoltaic Modules Optical Losses Due to Saharan Dust Deposition in Dakar,
1039 Senegal, West Africa. Smart Grid and Renewable Energy 11, 89.
1040 <https://doi.org/10.4236/sgre.2020.117007>

1041 Dubovik, O., King, M.D., 2000. A flexible inversion algorithm for retrieval of aerosol
1042 optical properties from Sun and sky radiance measurements. Journal of

1043 Geophysical Research: Atmospheres 105, 20673–20696.
1044 <https://doi.org/10.1029/2000JD900282>

1045 Engelstaedter, S., Tegen, I., Washington, R., 2006. North African dust emissions and
1046 transport. Earth-Science Reviews 79, 73–100.
1047 <https://doi.org/10.1016/j.earscirev.2006.06.004>

1048 Engelstaedter, S., Washington, R., 2007. Atmospheric controls on the annual cycle of
1049 North African dust. Journal of Geophysical Research: Atmospheres 112.
1050 <https://doi.org/10.1029/2006JD007195>

1051 Evans, M., Knippertz, P., Akpo, A., Allan, R.P., Amekudzi, L., Brooks, B., Chiu, J.C.,
1052 Coe, H., Fink, A.H., Flamant, C., Jegede, O.O., Leal-Liousse, C., Lohou, F.,
1053 Kalthoff, N., Mari, C., Marsham, J.H., Yoboué, V., Zumsprekel, C.R., 2018. Policy
1054 findings from the DACCIWA Project. Zenodo.
1055 <https://doi.org/10.5281/ZENODO.1476843>

1056 El Alani, O., Ghennioui, A., Ghennioui, H., Saint-Drenan, Y.-M., Blanc, P., 2020.
1057 Evaluation of 24-hours forecasts of global solar irradiation from IFS, GFS and
1058 McClear models.

1059 Fécan, F., Marticorena, B., Bergametti, G., 1998. Parametrization of the increase of the
1060 aeolian erosion threshold wind friction velocity due to soil moisture for arid and
1061 semi-arid areas. Annales Geophysicae 17, 149–157.
1062 <https://doi.org/10.1007/s00585-999-0149-7>

1063 Flamant, C., Chaboureaud, J.-P., Delanoë, J., Gaetani, M., Jamet, C., Lavaysse, C.,
1064 Bock, O., Borne, M., Cazenave, Q., Coutris, P., Cuesta, J., Menut, L., Aubry, C.,
1065 Benedetti, A., Bosser, P., Bounissou, S., Caudoux, C., Collomb, H., Donal, T.,
1066 Febvre, G., Fehr, T., Fink, A.H., Formenti, P., Araujo, N.G., Knippertz, P., Lecuyer,
1067 E., Andrade, M.N., Langué, C.G.N., Jonville, T., Schwarzenboeck, A., Takeishi, A.,
1068 2024. Cyclogenesis in the Tropical Atlantic: First Scientific Highlights from the
1069 Clouds–Atmospheric Dynamics–Dust Interactions in West Africa (CADDIWA) Field
1070 Campaign. Bulletin of the American Meteorological Society 105, E387–E417.
1071 <https://doi.org/10.1175/BAMS-D-23-0230.1>

1072 Gelaro, R., McCarty, W., Suárez, M.J., Todling, R., Molod, A., Takacs, L., Randles,
1073 C.A., Darmenov, A., Bosilovich, M.G., Reichle, R., Wargan, K., Coy, L., Cullather,
1074 R., Draper, C., Akella, S., Buchard, V., Conaty, A., Silva, A.M. da, Gu, W., Kim, G.-
1075 K., Koster, R., Lucchesi, R., Merkova, D., Nielsen, J.E., Partyka, G., Pawson, S.,
1076 Putman, W., Rienecker, M., Schubert, S.D., Sienkiewicz, M., Zhao, B., 2017. The
1077 Modern-Era Retrospective Analysis for Research and Applications, Version 2
1078 (MERRA-2). Journal of Climate 30, 5419–5454. <https://doi.org/10.1175/JCLI-D-16-0758.1>

1080 Giles, D.M., Sinyuk, A., Sorokin, M.G., Schafer, J.S., Smirnov, A., Slutsker, I., Eck, T.F.,
1081 Holben, B.N., Lewis, J.R., Campbell, J.R., Welton, E.J., Korkin, S.V., Lyapustin,
1082 A.I., 2019. Advancements in the Aerosol Robotic Network (AERONET) Version 3
1083 database – automated near-real-time quality control algorithm with improved cloud

1084 screening for Sun photometer aerosol optical depth (AOD) measurements.
1085 Atmospheric Measurement Techniques 12, 169–209. [https://doi.org/10.5194/amt-](https://doi.org/10.5194/amt-12-169-2019)
1086 [12-169-2019](https://doi.org/10.5194/amt-12-169-2019)

1087 Ginoux, P., Chin, M., Tegen, I., Prospero, J.M., Holben, B., Dubovik, O., Lin, S.-J.,
1088 2001. Sources and distributions of dust aerosols simulated with the GOCART
1089 model. Journal of Geophysical Research: Atmospheres 106, 20255–20273.
1090 <https://doi.org/10.1029/2000JD000053>

1091 Hauglustaine, D.A., Hourdin, F., Jourdain, L., Filiberti, M.-A., Walters, S., Lamarque, J.-
1092 F., Holland, E.A., 2004. Interactive chemistry in the Laboratoire de Météorologie
1093 Dynamique general circulation model: Description and background tropospheric
1094 chemistry evaluation. Journal of Geophysical Research: Atmospheres 109.
1095 <https://doi.org/10.1029/2003JD003957>

1096 Hersbach, H., Bell, B., Berrisford, P., Hirahara, S., Horányi, A., Muñoz-Sabater, J.,
1097 Nicolas, J., Peubey, C., Radu, R., Schepers, D., Simmons, A., Soci, C., Abdalla, S.,
1098 Abellan, X., Balsamo, G., Bechtold, P., Biavati, G., Bidlot, J., Bonavita, M., De
1099 Chiara, G., Dahlgren, P., Dee, D., Diamantakis, M., Dragani, R., Flemming, J.,
1100 Forbes, R., Fuentes, M., Geer, A., Haimberger, L., Healy, S., Hogan, R.J., Hólm,
1101 E., Janisková, M., Keeley, S., Laloyaux, P., Lopez, P., Lupu, C., Radnoti, G., de
1102 Rosnay, P., Rozum, I., Vamborg, F., Villaume, S., Thépaut, J.-N., 2020. The ERA5
1103 global reanalysis. Quarterly Journal of the Royal Meteorological Society 146, 1999–
1104 2049. <https://doi.org/10.1002/qj.3803>

1105 Holben, B.N., Eck, T.F., Slutsker, I., Tanré, D., Buis, J.P., Setzer, A., Vermote, E.,
1106 Reagan, J.A., Kaufman, Y.J., Nakajima, T., Lavenu, F., Jankowiak, I., Smirnov, A.,
1107 1998. AERONET—A Federated Instrument Network and Data Archive for Aerosol
1108 Characterization. Remote Sensing of Environment 66, 1–16.
1109 [https://doi.org/10.1016/S0034-4257\(98\)00031-5](https://doi.org/10.1016/S0034-4257(98)00031-5)

1110 Hu, X.-M., Klein, P.M., Xue, M., 2013. Evaluation of the updated YSU planetary
1111 boundary layer scheme within WRF for wind resource and air quality assessments.
1112 Journal of Geophysical Research: Atmospheres 118, 10,490-10,505.
1113 <https://doi.org/10.1002/jgrd.50823>

1114 Iacono, M.J., Delamere, J.S., Mlawer, E.J., Shephard, M.W., Clough, S.A., Collins,
1115 W.D., 2008. Radiative forcing by long-lived greenhouse gases: Calculations with
1116 the AER radiative transfer models. Journal of Geophysical Research: Atmospheres
1117 113. <https://doi.org/10.1029/2008JD009944>

1118 Inness, A., Ades, M., Agustí-Panareda, A., Barré, J., Benedictow, A., Blechschmidt, A.-
1119 M., Dominguez, J.J., Engelen, R., Eskes, H., Flemming, J., Huijnen, V., Jones, L.,
1120 Kipling, Z., Massart, S., Parrington, M., Peuch, V.-H., Razinger, M., Remy, S.,
1121 Schulz, M., Suttie, M., 2019. The CAMS reanalysis of atmospheric composition.
1122 Atmos. Chem. Phys. 19, 3515–3556. <https://doi.org/10.5194/acp-19-3515-2019>

1123 Jiménez, P.A., Dudhia, J., González-Rouco, J.F., Navarro, J., Montávez, J.P., García-
1124 Bustamante, E., 2012. A Revised Scheme for the WRF Surface Layer Formulation.

1125 Monthly Weather Review 140, 898–918. <https://doi.org/10.1175/MWR-D-11->
1126 [00056.1](https://doi.org/10.1175/MWR-D-11-00056.1)

1127 Jimenez, P.A., Hacker, J.P., Dudhia, J., Haupt, S.E., Ruiz-Arias, J.A., Gueymard, C.A.,
1128 Thompson, G., Eidhammer, T., Deng, A., 2016. WRF-Solar: Description and Clear-
1129 Sky Assessment of an Augmented NWP Model for Solar Power Prediction. Bulletin
1130 of the American Meteorological Society 97, 1249–1264.
1131 <https://doi.org/10.1175/BAMS-D-14-00279.1>

1132 Kaly, F., Marticorena, B., Chatenet, B., Rajot, J.L., Janicot, S., Niang, A., Yahi, H.,
1133 Thiria, S., Maman, A., Zakou, A., Coulibaly, B.S., Coulibaly, M., Koné, I., Traoré, S.,
1134 Diallo, A., Ndiaye, T., 2015. Variability of mineral dust concentrations over West
1135 Africa monitored by the Sahelian Dust Transect. Atmos. Res. 164–165, 226–241.
1136 <https://doi.org/10.1016/j.atmosres.2015.05.011>

1137 Kandler, K., Benker, N., Bundke, U., Cuevas, E., Ebert, M., Knippertz, P., Rodríguez, S.,
1138 Schütz, L., Weinbruch, S., 2007. Chemical composition and complex refractive
1139 index of Saharan Mineral Dust at Izaña, Tenerife (Spain) derived by electron
1140 microscopy. Atmospheric Environment 41, 8058–8074.
1141 <https://doi.org/10.1016/j.atmosenv.2007.06.047>

1142 Klose, M., Shao, Y., Karremann, M.K., Fink, A.H., 2010. Sahel dust zone and synoptic
1143 background. Geophysical Research Letters 37.
1144 <https://doi.org/10.1029/2010GL042816>

1145 Klüser, L., Killius, N., Gesell, G., 2015. APOLLO_NG – a probabilistic
1146 interpretation of the APOLLO legacy for AVHRR heritage channels. Atmospheric
1147 Measurement Techniques 8, 4155–4170. <https://doi.org/10.5194/amt-8-4155-2015>

1148 Kok, J.F., Adebisi, A.A., Albani, S., Balkanski, Y., Checa-Garcia, R., Chin, M., Colarco,
1149 P.R., Hamilton, D.S., Huang, Y., Ito, A., Klose, M., Li, L., Mahowald, N.M., Miller,
1150 R.L., Obiso, V., Pérez García-Pando, C., Rocha-Lima, A., Wan, J.S., 2021.
1151 Contribution of the world’s main dust source regions to the global cycle of desert
1152 dust. Atmos. Chem. Phys. 21, 8169–8193. [https://doi.org/10.5194/acp-21-8169-](https://doi.org/10.5194/acp-21-8169-2021)
1153 [2021](https://doi.org/10.5194/acp-21-8169-2021)

1154 Lefèvre M., 2022, CAMS solar radiation evaluation and quality assurance report #34,
1155 March-May 2021, ECMWF COPERNICUS REPORT,
1156 [https://atmosphere.copernicus.eu/sites/default/files/custom-uploads/EQC-solar/](https://atmosphere.copernicus.eu/sites/default/files/custom-uploads/EQC-solar/CAMS2_73_2021SC1_D1.3.1-2021Q4_RAD_validation_report_MAM2021_v1.pdf)
1157 [CAMS2_73_2021SC1_D1.3.1-2021Q4_RAD_validation_report_MAM2021_v1.pdf](https://atmosphere.copernicus.eu/sites/default/files/custom-uploads/EQC-solar/CAMS2_73_2021SC1_D1.3.1-2021Q4_RAD_validation_report_MAM2021_v1.pdf)

1158 Legates, D.R., McCabe, G.J., 2013. A refined index of model performance: a rejoinder.
1159 International Journal of Climatology 33, 1053–1056.
1160 <https://doi.org/10.1002/joc.3487>

1161 Léon, J.-F., Martiny, N., Merlet, S., 2020. A Multi Linear Regression Model to Derive
1162 Dust PM10 in the Sahel Using AERONET Aerosol Optical Depth and CALIOP
1163 Aerosol Layer Products. Remote Sensing 12, 3099.
1164 <https://doi.org/10.3390/rs12183099>

1165 Marsham, J.H., Parker, D.J., Grams, C.M., Grey, W.M.F., Johnson, B.T., 2008.
1166 Observations of mesoscale and boundary-layer circulations affecting dust uplift and
1167 transport in the Saharan boundary layer (preprint). [https://doi.org/10.5194/acpd-8-](https://doi.org/10.5194/acpd-8-8817-2008)
1168 [8817-2008](https://doi.org/10.5194/acpd-8-8817-2008)

1169 Marticorena, B., Bergametti, G., 1995. Modeling the atmospheric dust cycle: 1. Design
1170 of a soil-derived dust emission scheme. *Journal of Geophysical Research:*
1171 *Atmospheres* 100, 16415–16430. <https://doi.org/10.1029/95JD00690>

1172 Marticorena, B., Chatenet, B., Rajot, J.L., Traoré, S., Coulibaly, M., Diallo, A., Koné, I.,
1173 Maman, A., NDiaye, T., Zakou, A., 2010. Temporal variability of mineral dust
1174 concentrations over West Africa: analyses of a pluriannual monitoring from the
1175 AMMA Sahelian Dust Transect. *Atmos. Chem. Phys.* 10, 8899–8915.
1176 <https://doi.org/10.5194/acp-10-8899-2010>

1177 Marticorena, B., Dorego, G.S., Rajot, J.L., Bouet, C., Allègre, M., Chatenet, B., Féron,
1178 A., Gaimoz, C., Siour, G., Valorso, R., Diop, M., Der Ba, S., Rokhy N'Diaye, G.,
1179 Séné, M. & Thiam, A. (2021). Air temperature, Bambey, Senegal. [dataset]. Aeris.
1180 <https://doi.org/10.25326/263>

1181 Marticorena, B., Dorego, G.S., Rajot, J.L., Bouet, C., Allègre, M., Chatenet, B., Féron,
1182 A., Gaimoz, C., Maisonneuve, F., Siour, G., Valorso, R., Diop, M., Der Ba, S.,
1183 Rokhy N'Diaye, G., Séné, M. & Thiam, A. (2021). PM10 concentration, Bambey,
1184 Senegal. [dataset]. Aeris. <https://doi.org/10.25326/267>

1185 Masoom, A., 2021. Forecasting dust impact on solar energy using remote sensing and
1186 modeling techniques. *Solar Energy* 16.

1187 Mazzeo, A., Burrow, M., Quinn, A., Marais, E.A., Singh, A., Ng'ang'a, D., Gatari, M.J.,
1188 Pope, F.D., 2022. Evaluation of the WRF and CHIMERE models for the simulation
1189 of PM_{2.5} in large East African urban conurbations. *Atmospheric Chemistry and*
1190 *Physics* 22, 10677–10701. <https://doi.org/10.5194/acp-22-10677-2022>

1191 Menut, L., 2023. Variability and combination as an ensemble of mineral dust forecasts
1192 during the 2021 CADDIWA experiment using the WRF 3.7.1 and CHIMERE
1193 v2020r3 models. *Geoscientific Model Development* 16, 4265–4281.
1194 <https://doi.org/10.5194/gmd-16-4265-2023>

1195 Menut, L., Bessagnet, B., Briant, R., Cholakian, A., Couvidat, F., Mailler, S., Pennel, R.,
1196 Siour, G., Tuccella, P., Turquety, S., Valari, M., 2021. The CHIMERE v2020r1
1197 online chemistry-transport model. *Geoscientific Model Development* 14, 6781–
1198 6811. <https://doi.org/10.5194/gmd-14-6781-2021>

1199 Menut, L., Siour, G., Mailler, S., Couvidat, F., Bessagnet, B., 2016. Observations and
1200 regional modeling of aerosol optical properties, speciation and size distribution over
1201 Northern Africa and western Europe. *Atmos. Chem. Phys.* 16, 12961–12982.
1202 <https://doi.org/10.5194/acp-16-12961-2016>

1203 MODIS Atmosphere Science Team, 2017. MODIS/Terra Aerosol Cloud Water Vapor
1204 Ozone Daily L3 Global 1Deg CMG. https://doi.org/10.5067/MODIS/MOD08_D3.061

1205 Mostamandi, S., Ukhov, A., Engelbrecht, J., Shevchenko, I., Osipov, S., Stenchikov, G.,
1206 2023. Fine and Coarse Dust Effects on Radiative Forcing, Mass Deposition, and
1207 Solar Devices Over the Middle East. *Journal of Geophysical Research:*
1208 *Atmospheres* 128, e2023JD039479. <https://doi.org/10.1029/2023JD039479>

1209 Mueller, R., Pfeifroth, U., Traeger-Chatterjee, C., 2015. Towards Optimal Aerosol
1210 Information for the Retrieval of Solar Surface Radiation Using Heliosat. *Atmosphere*
1211 6, 863–878. <https://doi.org/10.3390/atmos6070863>

1212 Niu, G.-Y., Yang, Z.-L., Mitchell, K.E., Chen, F., Ek, M.B., Barlage, M., Kumar, A.,
1213 Manning, K., Niyogi, D., Rosero, E., Tewari, M., Xia, Y., 2011. The community
1214 Noah land surface model with multiparameterization options (Noah-MP): 1. Model
1215 description and evaluation with local-scale measurements. *Journal of Geophysical*
1216 *Research: Atmospheres* 116. <https://doi.org/10.1029/2010JD015139>

1217 Ochiegbu, D.C., 2021. Event of harmattan dust transport in Kano State of Nigeria.
1218 *IJSRP* 11, 205–210. <https://doi.org/10.29322/IJSRP.11.08.2021.p11628>

1219 Plain, N., Hingray, B., Mathy, S., 2019. Accounting for low solar resource days to size
1220 100% solar microgrids power systems in Africa. *Renewable Energy* 131, 448–458.
1221 <https://doi.org/10.1016/j.renene.2018.07.036>

1222 Prigent, C., Jiménez, C., Catherinot, J., 2012. Comparison of satellite microwave
1223 backscattering (ASCAT) and visible/near-infrared reflectances (PARASOL) for the
1224 estimation of aeolian aerodynamic roughness length in arid and semi-arid regions.
1225 *Atmospheric Measurement Techniques* 5, 2703–2712. <https://doi.org/10.5194/amt-5-2703-2012>

1226

1227 Prospero, J.M., Ginoux, P., Torres, O., Nicholson, S.E., Gill, T.E., 2002. Environmental
1228 Characterization of Global Sources of Atmospheric Soil Dust Identified with the
1229 Nimbus 7 Total Ozone Mapping Spectrometer (toms) Absorbing Aerosol Product.
1230 *Reviews of Geophysics* 40, 2-1-2–31. <https://doi.org/10.1029/2000RG000095>

1231 Qu, Z., Oumbe, A., Blanc, P., Espinar, B., Gesell, G., Gschwind, B., Klüser, L., Lefèvre,
1232 M., Saboret, L., Schroedter-Homscheidt, M., Wald, L., 2017. Fast radiative transfer
1233 parameterisation for assessing the surface solar irradiance: The Heliosat-4 method.
1234 *Meteorologische Zeitschrift* 33–57. <https://doi.org/10.1127/metz/2016/0781>

1235 Rajot, J.L., Abdourhamane Touré, A., Marticorena, B., Bouet, C., Allègre, M., Chatenet,
1236 B., Féron, A., Gaimoz, C., Siour, G., Valorso, R., Maman, A. & Zakou, A. (2010). Air
1237 temperature, Banizoumbou, Niger. [dataset]. AERIS. <https://doi.org/10.25326/210>

1238 Rajot, J.L., Boubacar, A., Marticorena, B., Bouet, C., Allègre, M., Chatenet, B., Féron,
1239 A., Gaimoz, C., Siour, G., Valorso, R., Coulibaly, S.B., Kouyaté, Z., Coulibaly, B.,
1240 Coulibaly, M., Koné, I. & Traoré, S. (2010). Air temperature, Cinzana, Mali.
1241 [dataset]. AERIS. <https://doi.org/10.25326/269>

1242 Rajot, J.L., Boubacar, A., Marticorena, B., Bouet, C., Allègre, M., Chatenet, B., Féron,
1243 A., Gaimoz, C., Maisonneuve, F., Siour, G., Valorso, R., Coulibaly, S.B., Kouyaté,
1244 Z., Coulibaly, B., Coulibaly, M., Koné, I. & Traoré, S. (2010). PM10 concentration,
1245 Cinzana, Mali. [dataset]. AERIS. <https://doi.org/10.25326/268>

1246 Redelsperger, J.-L., Diedhiou, A., Flamant, C., Janicot, S., Lafore, J.-P., Lebel, T.,
1247 Polcher, J., Bourlès, B., Caniaux, G., Rosnay, P. de, Desbois, M., Eymard, L.,
1248 Fontaine, B., Geneau, I., Ginoux, K., Hoepffner, M., Kane, C.S.E., Law, K.S., Mari,
1249 C., Marticorena, B., Mougin, É., Pelon, J., Peugeot, C., Protat, A., Roux, F., Sultan,
1250 B., Akker, E. van den, 2006. Amma, une étude multidisciplinaire de la mousson
1251 ouest-africaine. *La Météorologie* 54, 22. <https://doi.org/10.4267/2042/20098>

1252 Sawadogo, W., Bliefernicht, J., Fersch, B., Salack, S., Guug, S., Diallo, B., Ogunjobi,
1253 Kehinde.O., Nakoulma, G., Tanu, M., Meilinger, S., Kunstmann, H., 2023. Hourly
1254 global horizontal irradiance over West Africa: A case study of one-year satellite-
1255 and reanalysis-derived estimates vs. in situ measurements. *Renewable Energy*
1256 216, 119066. <https://doi.org/10.1016/j.renene.2023.119066>

1257 Sawadogo, W., Fersch, B., Bliefernicht, J., Meilinger, S., Rummmler, T., Salack, S., Guug,
1258 S., Kunstmann, H., 2024. Evaluation of the WRF-solar model for 72-hour ahead
1259 forecasts of global horizontal irradiance in West Africa: A case study for Ghana.
1260 *Solar Energy* 271, 112413. <https://doi.org/10.1016/j.solener.2024.112413>

1261 Schepanski, K., Tegen, I., Todd, M.C., Heinold, B., Bönisch, G., Laurent, B., Macke, A.,
1262 2009. Meteorological processes forcing Saharan dust emission inferred from MSG-
1263 SEVIRI observations of subdaily dust source activation and numerical models.
1264 *Journal of Geophysical Research: Atmospheres* 114.
1265 <https://doi.org/10.1029/2008JD010325>

1266 Schroedter-Homscheidt, M., Azam, F., Betcke, J., Harrieder, N., Lefevre, M., Saboret,
1267 L., Saint-Drenan, Y.-M., 2022. Surface solar irradiation retrieval from MSG/SEVIRI
1268 based on APOLLO Next Generation and HELIOSAT-4 methods. *Meteorologische*
1269 *Zeitschrift* 31, 455–476.

1270 Shao, Y., Lu, H., 2000. A simple expression for wind erosion threshold friction velocity.
1271 *Journal of Geophysical Research: Atmospheres* 105, 22437–22443.
1272 <https://doi.org/10.1029/2000JD900304>

1273 Skamarock, W.C., Klemp, J.B., Dudhia, J., Gill, D.O., Barker, D.M., Duda, M.G., Huang,
1274 X.-Y., Wang, W., Powers, J.G., n.d. A Description of the Advanced Research WRF
1275 Version 3.

1276 Sokolik, I.N., Toon, O.B., 1999. Incorporation of mineralogical composition into models
1277 of the radiative properties of mineral aerosol from UV to IR wavelengths. *J.*
1278 *Geophys. Res.* 104, 9423–9444. <https://doi.org/10.1029/1998JD200048>

1279 The Paris Agreement | UNFCCC [WWW Document], n.d. URL
1280 <https://unfccc.int/process-and-meetings/the-paris-agreement> (accessed 2.12.24).

1281 Thompson, G., Eidhammer, T., 2014. A Study of Aerosol Impacts on Clouds and
1282 Precipitation Development in a Large Winter Cyclone. *Journal of the Atmospheric*
1283 *Sciences* 71, 3636–3658. <https://doi.org/10.1175/JAS-D-13-0305.1>

1284 Tuccella, P., Menut, L., Briant, R., Deroubaix, A., Khvorostyanov, D., Mailler, S., Siour,
1285 G., Turquety, S., 2019. Implementation of Aerosol-Cloud Interaction within WRF-
1286 CHIMERE Online Coupled Model: Evaluation and Investigation of the Indirect

1287 Radiative Effect from Anthropogenic Emission Reduction on the Benelux Union.
1288 Atmosphere 10, 20. <https://doi.org/10.3390/atmos10010020>

1289 Vautard, R., Bessagnet, B., Chin, M., Menut, L., 2005. On the contribution of natural
1290 Aeolian sources to particulate matter concentrations in Europe: Testing hypotheses
1291 with a modelling approach. Atmospheric Environment 39, 3291–3303.
1292 <https://doi.org/10.1016/j.atmosenv.2005.01.051>

1293 Washington, R., Todd, M.C., 2005. Atmospheric controls on mineral dust emission from
1294 the Bodélé Depression, Chad: The role of the low level jet. Geophysical Research
1295 Letters 32. <https://doi.org/10.1029/2005GL023597>

1296 Washington, R., Todd, M.C., Lizcano, G., Tegen, I., Flamant, C., Koren, I., Ginoux, P.,
1297 Engelstaedter, S., Bristow, C.S., Zender, C.S., Goudie, A.S., Warren, A., Prospero,
1298 J.M., 2006. Links between topography, wind, deflation, lakes and dust: The case of
1299 the Bodélé Depression, Chad. Geophysical Research Letters 33.
1300 <https://doi.org/10.1029/2006GL025827>

1301 Wild, O., Zhu, X., Prather, M.J., n.d. Fast-J: Accurate Simulation of In- and Below-Cloud
1302 Photolysis in Tropospheric Chemical Models.

1303 Willis, P.T., Tattelman, P., 1989. Drop-Size Distributions Associated with Intense
1304 Rainfall. Journal of Applied Meteorology (1988-2005) 28, 3–15.

1305 Yahi, H., Marticorena, B., Thiria, S., Chatenet, B., Schmechtig, C., Rajot, J.L., Crepon,
1306 M., 2013. Statistical relationship between surface PM10 concentration and aerosol
1307 optical depth over the Sahel as a function of weather type, using neural network
1308 methodology. Journal of Geophysical Research: Atmospheres 118, 13,265-13,281.
1309 <https://doi.org/10.1002/2013JD019465>

1310 Yang, D., Bright, J.M., 2020. Worldwide validation of 8 satellite-derived and reanalysis
1311 solar radiation products: A preliminary evaluation and overall metrics for hourly data
1312 over 27 years. Solar Energy, Special Issue on Grid Integration 210, 3–19.
1313 <https://doi.org/10.1016/j.solener.2020.04.016>

1314 Yue, X., Wang, H., Liao, H., Fan, K., 2010. Simulation of dust aerosol radiative feedback
1315 using the GMOD: 2. Dust-climate interactions. Journal of Geophysical Research:
1316 Atmospheres 115. <https://doi.org/10.1029/2009JD012063>

1317 Yushchenko, A., De Bono, A., Chatenoux, B., Kumar Patel, M., Ray, N., 2018. GIS-
1318 based assessment of photovoltaic (PV) and concentrated solar power (CSP)
1319 generation potential in West Africa. Renewable and Sustainable Energy Reviews
1320 81, 2088–2103. <https://doi.org/10.1016/j.rser.2017.06.021>

1321 Zhang, L., Gong, S., Padro, J., Barrie, L., 2001. A size-segregated particle dry
1322 deposition scheme for an atmospheric aerosol module. Atmospheric Environment
1323 35, 549–560. [https://doi.org/10.1016/S1352-2310\(00\)00326-5](https://doi.org/10.1016/S1352-2310(00)00326-5)

1324 Ziane, A., Necaibia, A., Sahouane, N., Dabou, R., Mostefaoui, M., Bouraiou, A., Khelifi,
1325 S., Rouabhia, A., Blal, M., 2021. Photovoltaic output power performance
1326 assessment and forecasting: Impact of meteorological variables. Solar Energy 220,
1327 745–757. <https://doi.org/10.1016/j.solener.2021.04.004>